Modeling Wind-Induced Changes to Overturning Wave Shape

Falk Feddersen[1] †, Kentaro Hanson[2], Wouter Mostert[3], Adam Fincham[45]

[1]Scripps Institution of Oceanography, UCSD, La Jolla, CA, USA

[2]Program in Applied and Computational Mathematics, Princeton University, Princeton NJ, USA

[3]Department of Engineering Science, Oxford University, UK.

[4]Kelly Slater Wave Company, Los Angeles, CA, USA

[5]Department of Aerospace and Mechanical Engineering, University of Southern California, Los Angeles, CA

(Received xx; revised xx; accepted xx)

Depth-limited overturning wave shape affects water turbulence and sediment suspension. Experiments have shown that wind affects shoaling and overturning wave shape, with uncertain mechanism. Here we study wind effects (given by wind Reynolds number) on solitary wave shoaling and overturning with the 2-phase DNS model Basilisk run in two-dimensions for a fixed wave Reynolds and Bond number and steep bathymetry. The propagating solitary wave sheds a 2D turbulent air wake and has nearly uniform speed over the rapidly varying bathymetry for all wind. The solitary wave face slope is clearly influenced by wind. Changes to shoaling solitary wave shape are consistent with previous studies. As overturning jet impacts, wind-dependent differences in overturn shape are evident and quantified. The nondimensional breakpoint location and overturn area have similar wind dependence as experiment, albeit requiring larger wind speed. The overturn aspect ratio has opposite wind dependence as experiment. During shoaling, the surface viscous stresses are negligible relative to pressure. Surface tension effects are also small but grow rapidly near overturning. In a wave frame of reference, surface pressure is low in the lee and contributes 2-5% to the velocity potential rate of change in the surface dynamic boundary condition, which, integrated over time changes the wave shape. Reasons the overturn aspect ratio is different than experiment and why a stronger simulated wind is required are explored. The dramatic wind-effects on overturning jet area, and thus to the available overturn potential energy, make concrete the implications of wind-induced changes to wave shape.

1. Introduction

As they approach shore, shoaling waves change shape becoming steeper with narrower peaks and more pitched forward (e.g. Elgar & Guza 1985). Once sufficiently steepened, depth-limited wave breaking occurs with wave overturning, and subsequently the overturn jet impacts the water-surface in front of the wave. Depth-limited wave breaking is often qualitatively categorized into spilling and plunging (e.g. Peregrine 1983), where spilling waves have very small overturns and plunging waves have larger overturns. Bathymetry along with offshore wave height and wavelength are well understood (e.g. via the Iribarren number) to be important in setting spilling or plunging wave breaking (e.g. Peregrine 1983). For example, larger planar beach slope β leads to larger overturns (Grilli *et al.* 1997; Mostert & Deike 2020; O'Dea *et al.* 2021). Across laboratory and field observations, the wave overturn shape is important in the resulting splash up and bubble entrainment (Chanson & Jaw-Fang 1997; Yasuda *et al.* 1999; Blenkinsopp & Chaplin 2007), water column turbulence (Ting & Kirby 1995, 1996; Aagaard *et al.* 2018), sediment suspension

† Email address for correspondence: ffeddersen@ucsd.edu

(e.g. Aagaard *et al.* 2018), and wave impact forces on engineered structures (Bullock *et al.* 2007). Similarly in numerical simulations of deep-water and depth-limited wave breaking, the geometry of wave overturning impacts air entrainment, vorticity generation, and pathways of turbulent dissipation (e.g. Lubin *et al.* 2006; Derakhti & Kirby 2014; Mostert *et al.* 2022). Thus, understanding the factors that affect the shape of overturning waves is important to a range of processes.

In deep water, wind is well understood to lead to surface gravity wave growth and decay (e.g. Miles 1957; Phillips 1957). However, wind can also change wave shape in both deep (Leykin *et al.* 1995; Zdyrski & Feddersen 2020) and shallow (Zdyrski & Feddersen 2021) water, as well as shoaling waves (Feddersen & Veron 2005; Sous *et al.* 2021; Zdyrski & Feddersen 2022). In laboratory studies, onshore wind results in wave breaking in deeper water (farther offshore) (Douglass 1990; Sous *et al.* 2021), with the opposite for offshore wind. Feddersen *et al.* (2023) studied the explicit dependence of overturn wave shape on wind at the Surf Ranch, a wave basin designed for surfing. Field-scale shoaling solitary wave with height ≈ 2.25 m propagated at $C = 6.7\ \mathrm{m\,s^{-1}}$ and overturned. The cross-wave component of wind U, measured 16 m above the water surface, varied from onshore to offshore with realistic $-1.2 < U/C < 0.7$. The non-dimensionalized breakpoint location was inversely related to U/C, consistent with Douglass (1990). The nondimensional overturn area A/H_b^2, where H_b is breaking wave height, and overturn aspect ratio were also inversely related to U/C, with smaller area and overturns for increasing onshore wind (positive U/C). For increasing offshore wind, A/H_b^2 was approximately uniform. The nondimensional overturn parameters varied by a factor of two for the observed U/C indicating that the wind has a significant effect on overturn shape. However, the mechanism by which wind effects these geometric changes is uncertain. For example, the pressure profiles induced by the wind on the different parts of the evolving wave, along with the general flow structure over and around the wave, remain unknown.

Numerical modeling offers a promising avenue for investigating wind effects on shoaling and overturning wave shape. Advances in two phase numerical modeling both DNS and LES has enabled significant advances in understanding deep (Lubin *et al.* 2019; Mostert *et al.* 2022) and shallow water wave breaking (e.g. Mostert & Deike 2020; Boswell *et al.* 2023; Liu *et al.* 2023). Similar advances have occurred in the study of wind and wave interactions in deep water (e.g. Hao & Shen 2019; Wu *et al.* 2022). However, the interaction of shoaling and overturning waves and wind has largely not been studied. Numerical studies using two-phase RANS solvers of wind-forced solitary (Xie 2014) and progressive (Xie 2017) waves have seen a wind-induced shift in breakpoint location analogous to laboratory experiments. However, the effect of wind on overturning wave shape has yet to be studied.

Here, we study the wind effects on solitary wave shoaling and overturning for a model domain similar to that of Feddersen *et al.* (2023) using the two-phase numerical model Basilisk run in two-dimensions. In section 2, the model setup is described, the key nondimensional parameters including wind Reynolds number Re^* are defined, and the relationship between modeled air velocity $\langle \bar{U} \rangle / C$ and Re^* is discussed. In Section 3.1, the qualitative features of the shoaling solitary wave and air vorticity are examined for strong onshore and offshore wind. The statistics of solitary wave shoaling under strong onshore and offshore wind are described in section 3.2. Overturn wave shape is quantified by geometrical parameters defined at the moment of jet impact (Section 3.3). The relationship of the nondimensional geometrical parameters (defined in Section 3.4) to Re^* is examined (Section 3.5). The relative strength of viscous stresses and pressure at the air-water interface is examined in Section 3.6, and the terms of the surface dynamic boundary condition including pressure variations and surface tension are analyzed in Section 3.7. We discuss the shoaling results relative to previous studies, examine potential reasons for the differences between our results here and those of field-scale experiments, and consider implications in Section 4. Section 5 provides a summary.

2. Methods

We numerically simulate in two dimensions (2D) the shoaling and overturning of a solitary wave with the two-phase incompressible Navier-Stokes equations using the open-source Basilisk software package (Popinet 2003, 2009, 2018) for solving partial differential equations on an adaptively refined grid. Basilisk has been extensively used to model wave breaking (Deike *et al.* 2015, 2016; Mostert & Deike 2020; Mostert *et al.* 2022), as well as wave interactions with wind (Wu & Deike 2021; Wu *et al.* 2022).

2.1. *Formulation and Governing Equations*

The governing equations are the two-phase (water and air) Navier-Stokes equations in 2D, given as

$$
\begin{aligned}
\frac{\partial \rho}{\partial t} + \nabla \cdot (\rho \mathbf{u}) &= 0 \\
\rho \left(\frac{\partial \mathbf{u}}{\partial t} + \mathbf{u} \cdot \nabla \mathbf{u} \right) &= -\nabla p + \rho \mathbf{g} + \nabla \cdot (2\mu \mathbf{D}) + \sigma \kappa \mathbf{n} \delta_s \\
\nabla \cdot \mathbf{u} &= 0
\end{aligned}
\tag{2.1}
$$

where $\mathbf{u}, \sigma, \kappa, \mathbf{D}, \mathbf{g}$ are the fluid velocity, surface tension, curvature of the interface, deformation tensor, and acceleration due to gravity, respectively. In component form, the 2D fluid velocity $\mathbf{u} = (u, w)$ where u and w are the horizontal and vertical velocities, respectively. For each fluid, the water and air density $(\rho_{\mathrm{w}}, \rho_{\mathrm{a}})$ and dynamic viscosity $(\mu_{\mathrm{w}}, \mu_{\mathrm{a}})$ are uniform. A volume-of-fluid (VOF) advection scheme with a color function f is used to capture and advect the air-water interface in a momentum-conserving implementation. Hence for two-phase mixtures, ρ and μ are represented by

$$
\begin{aligned}
\rho &= f \rho_{\mathrm{w}} + (1 - f) \rho_{\mathrm{a}} \\
\mu &= f \mu_{\mathrm{w}} + (1 - f) \mu_{\mathrm{a}}
\end{aligned}
\tag{2.2}
$$

where f is interpreted as the liquid volume fraction ($f = 1$ for water, $f = 0$ for air). The water-to-air ratio for ρ and μ are important nondimensional parameters and are here held fixed at $\rho_{\mathrm{a}}/\rho_{\mathrm{w}} = 0.001$ and $\mu_{\mathrm{a}}/\mu_{\mathrm{w}} = 0.018$. The air-water interface requires continuity of velocity and stress, including surface tension. Surface tension as the interfacial force $\sigma \kappa \mathbf{n} \delta_s$ is determined from the Dirac delta δ_s on the interface and the unit normal vector $\mathbf{n}$. This formulation is expressed in Popinet (2018), alongside the implementation of gravity as an interfacial force. In (2.1), we substitute

$$
\rho \mathbf{g} \rightarrow (\rho_{\mathrm{a}} - \rho_{\mathrm{w}})(\mathbf{g} \cdot \mathbf{x}) \mathbf{n} \delta_s
$$

which are equal, up to a difference in the pressure field. The reduced gravity implementation avoids the appearance of spurious velocities and unphysical energy production near the air-water interface (Wroniszewski *et al.* 2014).

The two phase incompressible Navier-Stokes equations are solved on an adaptive Cartesian mesh using the Bell-Colella-Glaz projection method (Bell *et al.* 1989) with the VOF scheme described above, allowing for a sharp interface between phases (Fuster & Popinet 2018; López-Herrera *et al.* 2019; van Hooft *et al.* 2018). The bathymetry is represented with an additional volume fraction field as an embedded boundary (Johansen & Colella 1998). Surface tension is implemented using the continuum-surface-force approach due to Brackbill *et al.* (1992).

2.1.1. *Model Domain and Boundary Conditions*

The model domain (figure 1) is similar to to that used in Boswell *et al.* (2023) with modifications to be analogous to the bathymetry of the Surf Ranch (Feddersen *et al.* 2023). In the offshore region,

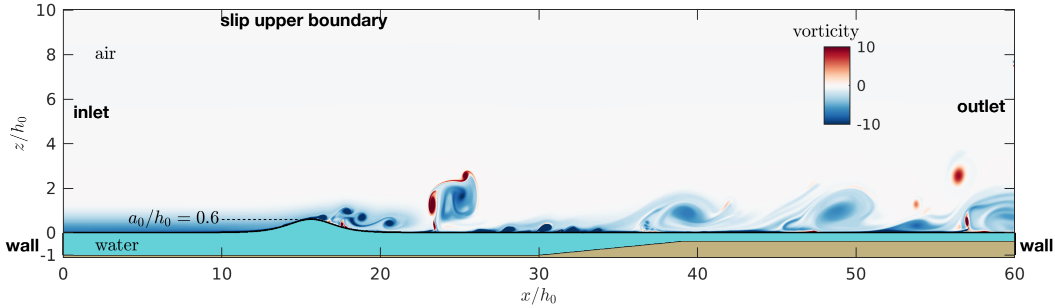

Figure 1. The simulation domain just after initialization as a function of nondimensional horizontal x/h_0 and vertical z/h_0 coordinates. The brown region represents the bathymetry, the aqua blue is water, the air-sea interface is indicated by the black curve, and air vorticity is given by the colorbar. The deeper flat water depth at $x/h_0 < 30$ has depth h_0 such that the bed is located at $z/h_0 = -1$. The shallow flat region has depth $h_s/h_0 = 0.371$, and the bathymetric slope connecting these two regions has slope $\beta = 0.0693$. The solitary wave initial condition parameters are $a_0/h_0 = 0.6$ and $x_0/h_0 = 15$. The height of the air domain is $h_a/h_0 = 10$. This example is for onshore wind and $\mathrm{Re}^* = 2400$. The air inlet and outlet boundary conditions, together with the slip upper boundary condition are noted. The air vorticity is from the initial condition derived from the air-only precursor simulation.

the bathymetry is flat with depth h_0 and the total cross-shore (x) domain size is $L_x = 60h_0$. The offshore flat bathymetry extends for a x/h_0-distance of 30. At $x/h_0 = 30$, the bathymetry slopes upward with a slope of $\beta = 0.0693$ over a x/h_0-distance of 9.08 to a shallow depth $h_s/h_0 = 0.371$, which then extends a x/h_0-distance of nearly 20. The bathymetric slope is a key non-dimensional parameter well understood to affect overturn shape (e.g. Grilli *et al.* 1997; Mostert & Deike 2020; O'Dea *et al.* 2021). Here, β is held fixed to the Surf Ranch bathymetric slope projected in the direction of wave propagation (Feddersen *et al.* 2023) in order to isolate the wind-effects on overturning shape. The bathymetry has a no-slip boundary condition for fluid velocity. At the ends of the model domain at $x = 0$ and $x/h_0 = 60$, vertical walls extend from the bathymetry to the still water depth at $z/h_0 = 0$, with associated $u = 0$ and no-slip boundary conditions. The air domain extends vertically from the water surface (mostly near $z/h_0 = 0$) to $z/h_0 = h_a/h_0 = 10$, where a "ceiling", with a free-slip boundary condition, is placed on the domain (figure 1). Between $0 < z/h_0 < 10$, at the left and right boundaries ($x/h_0 = 0$ and $x/h_0 = 60$, figure 1) open boundaries allow for air flow in and out of the domain. The inlet and outlet location vary depending on the wind direction. For onshore winds, the left side is the inlet and for offshore winds, the right side is the inlet. A Neumann condition is placed on the dynamic pressure, $\partial p/\partial x = 0$, on the inlet, and a Dirichlet dynamic pressure condition $p = 0$ is placed on the outlet, both uniformly in the vertical.

2.1.2. *Water Solitary Wave Initial Condition and Wave-related Nondimensional Parameters*

The simulation free surface initial condition η_0 is a solitary wave solution to the KdV equation (e.g. Ablowitz 2011),

$$\eta_0(x) = a_0 \operatorname{sech}^2\left(\frac{(x - x_0)}{h_0}\left(\frac{3a_0/h_0}{4(1 + a_0/h_0)}\right)^{1/2}\right), \tag{2.3}$$

that is formally a water wave solution for small a_0/h_0. The water velocity initial condition associated with this free surface is,

$$u(x) = \frac{C\eta(x)}{h_0 + \eta(x)}$$
$$w(x, z) = C\frac{z + h_0}{h_0 + \eta(x)}\left(\frac{\partial\eta}{\partial x}(x)\right)\left(1 - \frac{\eta(x)}{h_0 + \eta(x)}\right), \tag{2.4}$$

where $C = \sqrt{(gh_0)(1 + a_0/h_0)}$ is the solitary wave propagation speed, and the vertical velocity is derived from continuity. For all simulations, the non-dimensional solitary wave amplitude is set similar to that generated at the Surf Ranch (Feddersen *et al.* 2023) at $a_0/h_0 = 0.6$ and the center of the solitary wave is located at $x_0/h_0 = 15$ (figure 1), implying a non-dimensional propagation speed $\tilde{C} = C/\sqrt{gh_0} = 1.265$.

Once the simulation starts, the solitary wave propagates in the $+x$ direction with speed close to $\tilde{C}$ and adjusts, as the initial condition (2.3 & 2.4) is not an exact solution of the two-phase Navier-Stokes equations. However, this initial condition generates minor trailing transients (Mostert & Deike 2020), which nonetheless do not affect shoaling or overturning characteristics. The solitary wave then shoals over the rapidly varying bathymetry and eventually overturns in the shallow flat region (figure 1). From the initial condition solitary wave parameters, a wave Reynolds number is defined as (Mostert & Deike 2020; Boswell *et al.* 2023)

$$\mathrm{Re_w} = \frac{\sqrt{gh_0^3}}{\nu_w} \tag{2.5}$$

where $\nu_w = \mu_\mathrm{w}/\rho_\mathrm{w}$ is the kinematic viscosity of water, and the linear shallow water phase speed $\sqrt{gh_0}$ and offshore depth h_0 are used as velocity and length-scales. Here, as in previous studies (Mostert & Deike 2020; Boswell *et al.* 2023), we keep the wave Reynolds number fixed at $\mathrm{Re_w} = 4 \times 10^4$. The Bond number Bo is also an important nondimensional parameter tracking the importance of surface tension. For a solitary wave, Bo is defined as (Mostert & Deike 2020),

$$\mathrm{Bo} = \frac{(\rho_\mathrm{w} - \rho_\mathrm{a})gh_0^2}{\sigma} \tag{2.6}$$

where h_0 is chosen as the length-scale because solitary wave width scales with the water depth (2.3). Here, we have a fixed Bo = 4000 slightly larger than the Bo = 1000 used in previous shoaling and breaking solitary wave studies (Mostert & Deike 2020; Boswell *et al.* 2023). A nondimensional time is defined as

$$\tilde{t} = \left(\frac{g}{h_0}\right)^{1/2} t, \tag{2.7}$$

with $\tilde{t} = 0$ defined at moment when the solitary wave begins propagating. Variables with a tilde denote nondimensional variables.

2.1.3. *Air Initial Condition*

The air-phase initial condition used for the shoaling solitary wave problem is defined by first running an air-phase-only precursor simulation (described in more detail in Appendix A) analogous to the precursor simulation of Wu *et al.* (2022). The precursor simulation solves for the airflow over a solitary wave in a reference frame of the solitary wave propagating with constant speed, with no-slip boundary conditions at the wave surface matching the solitary wave fluid velocity (2.4).This choice of boundary conditions at the wave surface in the precursor simulation ensures that, at the beginning of the two-phase shoaling simulation, the air-phase velocity field is consistent with a moving solitary wave. To force the wind, the air-only simulation has an external, spatially and temporally uniform pressure gradient applied, specified by a nominal friction velocity u_*

$$\frac{\partial p}{\partial x} = \frac{\rho_{\mathrm{a}} u_* |u_*|}{h_a}. \tag{2.8}$$

We characterize the airflow with a wind Reynold number (Wu *et al.* 2022)

$$\mathrm{Re}^* = \frac{u_* h_a}{\nu_a}, \tag{2.9}$$

where ν_a is the kinematic viscosity of air and $h_a/h_0 = 10$ is the thickness of the undisturbed air layer. For offshore winds (air flow opposite of solitary wave propagation direction), u_* is negative as is the resulting Re^*. The velocity field in the air phase at the conclusion of the precursor simulation is then used as the initial condition for the shoaling wave problem, which solves the full two-phase system in a fixed reference frame. During the two-phase simulations, the forcing pressure gradient discussed above is removed. As the solitary wave fully overturns for all Re^* by $\tilde{t} = 21$, the wind does not have sufficient time to decelerate in any meaningful way.

2.1.4. *Recapitulation of Nondimensional Parameters*

The simulations are performed in nondimensional variables and coordinates. Most of the nondimensional parameters are held fixed and key fixed parameters are recapitulated here. The air-water density ratio is $\rho_{\mathrm{a}}/\rho_{\mathrm{w}} = 0.001$. The air-water dynamic viscosity ratio is $\mu_{\mathrm{a}}/\mu_{\mathrm{w}} = 0.018$. The initial solitary wave amplitude is $a_0/h_0 = 0.6$ corresponding to a wave Reynolds number of $\mathrm{Re}_{\mathrm{w}} = 4 \times 10^4$. The beach slope is $\beta = 0.0693$. Note, for a kinematic viscosity of water $\nu_w = 10^{-6}$ m^2 s^{-1}, the wave Reynolds number implies a $h_0 = 0.055$ m, a solitary wave amplitude of $a_0 = 0.033$ m, and a solitary wave speed of $C = 0.93$ m s^{-1}. For the field scale solitary waves at the Surf Ranch (Feddersen *et al.* 2023), the equivalent $\mathrm{Re}_{\mathrm{w}} = 1.4 \times 10^7$. Here, the $\mathrm{Bo} = 4000$ is four times larger than that previously in shoaling and breaking solitary wave studies (Mostert & Deike 2020; Boswell *et al.* 2023). We note that the Bond number for the field scale solitary waves at the Surf Ranch is $\mathrm{Bo} = 3.6 \times 10^5$, almost a factor 100× larger than used here. Thus, the present simulations are not at field scale with respect to viscous effects or surface tension effects, which will be explored in the Discussion. The nondimensional wind friction velocity Re^* (2.9) is hypothesized to be important in setting wind effects on overturning shape and is varied over $\mathrm{Re}^* = \{-1800, -1200, -600, 0, 600, 1200, 1800, 2400\}$.

2.1.5. *Adaptive Mesh Refinement and Convergence*

Basilisk uses adaptive mesh refinement (AMR) to reduce computational cost. Refinement is based on the error of the velocity, VOF field, and solid boundary approximation, using a wavelet estimation algorithm. The AMR approach used in Basilisk is described in van Hooft *et al.* (2018) . The Basilisk domain is a $L_x/h_0 \times L_x/h_0$ square, with quadtree subdivision, ensuring that all grid cells are square. A maximum of 14 levels of refinement was chosen so that the effective minimum mesh size becomes $\Delta x/h_0 = (L_0/h_0)/2^{14} = 3.7 \times 10^{-3}$, corresponding to a minimum dimensional mesh size of 0.2 mm, for a dimensional depth of $h_0 = 0.055$ m. Although the domain is a square, the vertical domain of interest is about 1/6 of the total vertical domain. The bathymetry is embedded as a bottom boundary condition within the domain, and the domain below the bathymetry remains essentially unresolved reducing computational cost.

Previous studies with Basilisk of breaking solitary waves (Mostert & Deike 2020; Boswell *et al.* 2023) found that for similar size model domains ($L_x/h_0 = 50$), the model solutions were grid-converged across both pre- and post-wave breaking regimes at 14 levels of refinement. Here, we are only interested in the model solutions up until the point that the overturning jet impacts the water surface in front of it, that is pre-breaking. In terms of refinement, the pre-breaking regime is much less demanding. As in figure 1, the scales of the 2D wind turbulence are not small. Therefore with 14 levels of refinement, the pre-breaking solution is expected to be converged.

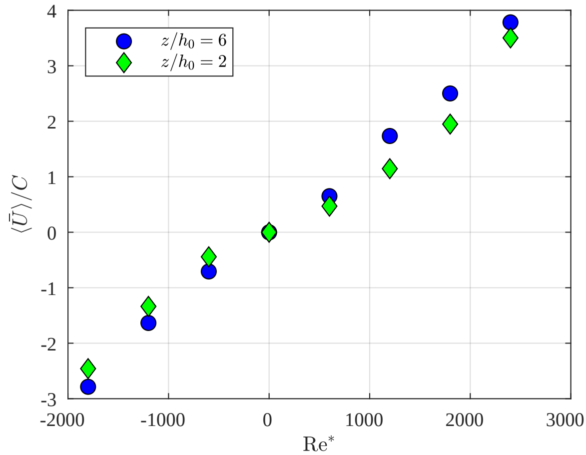

Figure 2. Nondimensional x- and time-averaged wind speed $\langle\bar{U}\rangle/C$ (2.14) versus wind Reynolds number Re^* (2.9) at heights $z/h_0 = 6$ (blue) and $z/h_0 = 2$ (green diamonds).

2.1.6. *Model output*

Model output is stored every $\Delta\tilde{t} = 0.05$ for $\tilde{t} < 18$ and every $\Delta\tilde{t} = 0.01$ for $\tilde{t} \geqslant 18$ to ensure that the wave overturn is temporally well-resolved in the model output. From model output, fluid volume fraction f, velocity, vorticity, pressure are estimated on a regular grid over the domain. In addition, the air-water interface η, as well as interface velocities are output at the AMR resolution. Pressure at the interface can be noisy due to the surface tension term. Thus interface air pressure is estimated in the air, a distance $\Delta = 0.01$ normal to the surface interface. This distance is approximately 2.7× the minimum grid resolution at 14 levels of refinement. In addition we also output u and w in the air on a diamond stencil centered on the location of pressure with stencil leg distance 0.004 that allow 2nd order estimates of $\partial u/\partial x$, $\partial u/\partial z$, $\partial w/\partial x$ and $\partial w/\partial z$ over a separation of 0.008. As the wave propagates and shoals, most of the time the air-water interface η is single-valued with x/h_0. Once the overturning jet forms, η is no longer single valued. For the times when single-valued, we define $\eta(x,t)$ as the air-water interface. Nondimensional water and air kinetic $(K_\mathrm{w}, K_\mathrm{a})$ and potential $(P_\mathrm{w}, P_\mathrm{a})$ energies are estimated as (e.g. Mostert *et al.* 2022)

$$K_\mathrm{w,a} = \int_{V_\mathrm{w,a}} \frac{\rho}{2}|\mathbf{u}|^2 \mathrm{d}V, \quad P_\mathrm{w,a} = \int_{V_\mathrm{w,a}} \rho g z \mathrm{d}V. \tag{2.10}$$

where the integrals are over the water or air regions, respectively. The potential energy is referenced relative to the potential energy at $t = 0$. The water and air energy (kinetic plus potential) is thus

$$E_\mathrm{w,a} = K_\mathrm{w,a} + P_\mathrm{w,a}. \tag{2.11}$$

Nondimensional water energy $\tilde{E}_\mathrm{w}$ is then given by

$$\tilde{E}_\mathrm{w} = \frac{E_\mathrm{w}}{\rho_w g h_0^3}. \tag{2.12}$$

2.2. *Relationship between wind speed and wind Reynolds number* Re^*

Before describing the evolution of the shoaling and overturning solitary wave under the effect of varying wind, we examine the dependence of model air velocity (wind) to Re^*. We will average the air velocity to have a single wind metric to compare with Re^*. The first averaging operator is the model-domain x-averaged wind velocity $\bar{U}(z/h_0, \tilde{t})$, defined as,

$$\bar{U}(z/h_0, \tilde{t}) = \frac{1}{L_x/h_0} \int_0^{L_x/h_0} u(x/h_0, z/h_0, \tilde{t})\, \mathrm{d}(x/h_0) \tag{2.13}$$

where $L_x/h_0 = 60$ is the length of the model domain (figure 1). As will be seen, the earliest solitary wave overturning occurs at $\tilde{t} = 19.13$. Thus, we define the period for time-averaging over $1 < \tilde{t} < 19$, which represents time-period of solitary wave evolution prior to overturning. During this time-period, the wind was largely steady. The time- and x-averaged air velocity $\langle \bar{U} \rangle$ is defined as

$$\langle \bar{U} \rangle (z/h_0) = \frac{1}{18} \int_1^{19} \bar{U}(z/h_0, \tilde{t})\, \mathrm{d}\tilde{t}, \tag{2.14}$$

is only a function of the vertical z/h_0, and is evaluated only for $z/h_0 \geqslant 1$ which is always air. We define the nondimensional wind speed as $\langle \bar{U} \rangle / C$.

We compare Re* and $\langle \bar{U} \rangle / C$ at two vertical locations $z/h_0 = \{2, 6\}$ (figure 2). The first location $z/h_0 = 2$ is representative of near-surface wind but is still at least two solitary wave amplitudes a_0/h above the air-water interface. The second $z/h_0 = 6$ represents the height of wind measurements in the field-scale experiments (Feddersen *et al.* 2023). For $z/h_0 = 6$, $\langle \bar{U} \rangle / C$ is largely linear with Re* (figure 2, circles) with $\langle \bar{U} \rangle / C = 3.8$ for Re$^* = 2400$ and $\langle \bar{U} \rangle / C = -2.8$ for Re$^* = -1800$. The linear relationship indicates that the stress is not due to turbulence and that Re* is a proxy for $\langle \bar{U} \rangle / C$. At $z/h_0 = 2$, $\langle \bar{U} \rangle / C$ is slightly weaker than at $z/h_0 = 6$ and has a weak quadratic trend (green diamonds in figure 2) with $\langle \bar{U} \rangle / C = 3.5$ at Re$^* = 2400$ and $\langle \bar{U} \rangle / C = -2.5$ at Re$^* = -1800$. At both z/h_0, the model $\langle \bar{U} \rangle / C$ range is larger than in field-scale observations where significant wind-effects on wave overturns occurred over $-1.2 < U/C < 0.8$. Based on the $\langle \bar{U} \rangle / C$ and Re* relationship (figure 2), this corresponds to $|\mathrm{Re}^*| < 1200$. Although modeling results will be analyzed using Re*, we will keep this relationship in mind.

3. Results

3.1. *Description of solitary wave transformation under wind*

We now present qualitative features of the solitary wave shoaling for the strongest onshore (Re$^* = 2400$) and offshore (Re$^* = -1800$) wind (figure 3) at two different times during shoaling. For both Re*, the modeled solitary wave speed is slightly faster than the small a_0/h_0 analytic $\tilde{C} = 1.265$. Onshore and offshore wind implies wind blowing in the $+x$ and $-x$ directions, respectively. The conventions used are as follows. Front and back of the solitary wave are in relation to the direction of $+x$ solitary wave propagation. Upstream and lee of the solitary wave are in relation to the airflow direction. At $\tilde{t} = 14.0$, the Re$^* = 2400$ solitary wave has propagated up the slope and has amplified from initial amplitude $a_0/h_0 = 0.6$ to a peak $\eta_{\mathrm{pk}}/h_0 = 0.71$ at $x_{\mathrm{pk}}/h_0 = 33.2$ (figure 3a). Wind is in the direction of solitary wave propagation and is faster than the solitary wave speed with $\langle \bar{U} \rangle / C \approx 3.4$ at at $z/h_0 = 2$ (figure 2). The shoaling solitary wave has also changed shape asymmetrically, characteristic of shoaling solitary waves (e.g. Knowles & Yeh 2018; Mostert & Deike 2020; Zdyrski & Feddersen 2022). The asymmetric front-face minimum steepness (slope) $\min(\partial\eta/\partial x) = -0.46$ and the back-face maximum slope $|\partial\eta/\partial x| = 0.32$, both larger than initial solitary wave maximum slope magnitude $|\partial\eta/\partial x| = 0.25$, indicate solitary wave shoaling. Upstream of the solitary wave, the airflow is laminar with the strongest negative vorticity concentrated at the air water interface. In the lee of the solitary wave, the airflow has separated and strong turbulence and turbulent ejections are present near the front face of the wave with positive and negative nondimensional vorticity near 10. At $\tilde{t} = 14.00$, the Re$^* = -1800$ solitary wave has propagated up the slope with maximum $\eta_{\mathrm{pk}}/h_0 = 0.68$ at $x_{\mathrm{pk}}/h_0 \approx 33.0$ (figure 3b), slightly slower than for the Re$^* = 2400$ simulation. The wind blows counter the direction of solitary

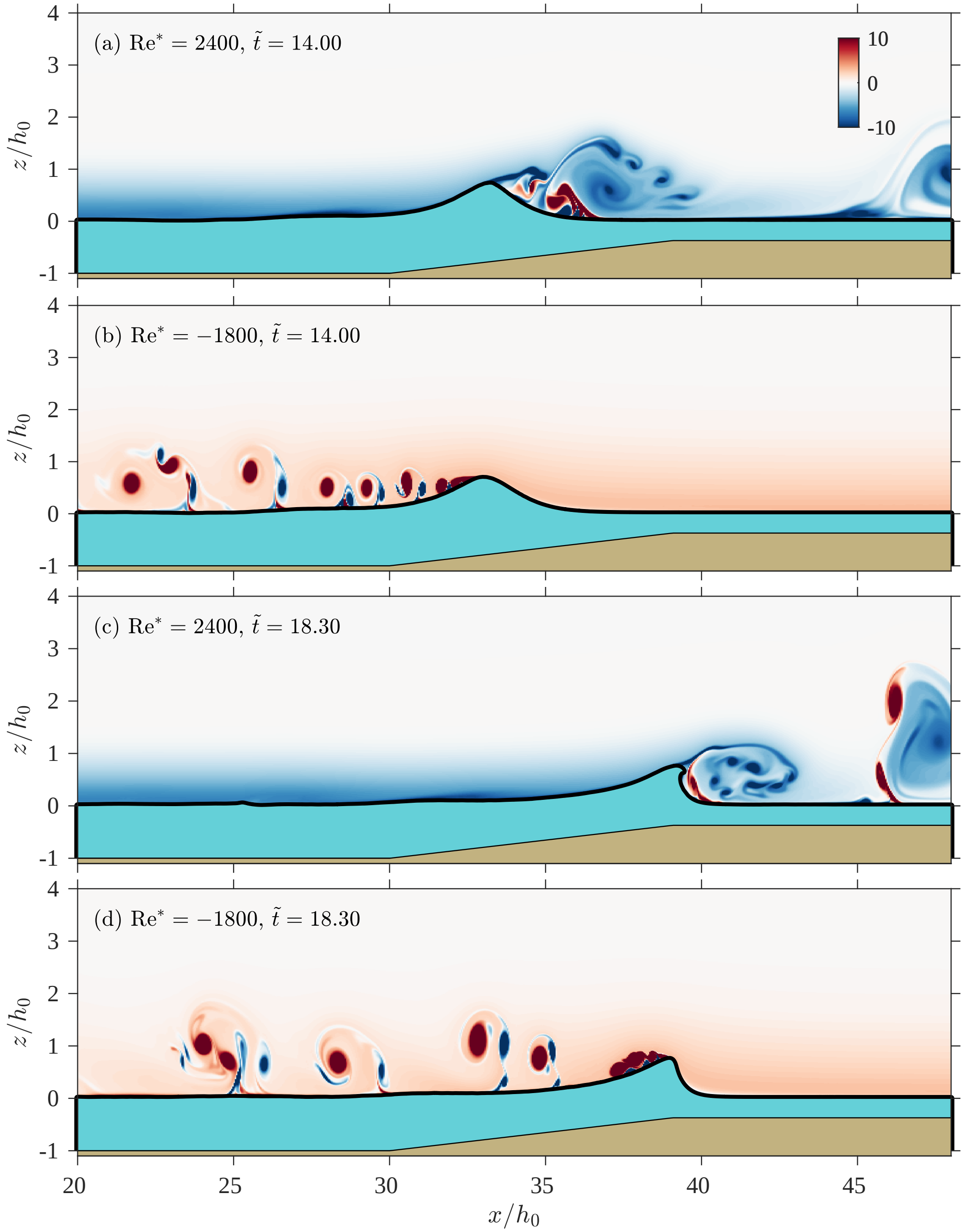

Figure 3. The solitary wave in water (aqua blue) shoaling over the bathymetry (brown) with overlaid air vorticity as a function of horizontal x/h_0 and vertical z/h_0 coordinates for times (a,b) $\tilde{t}$ = 14 and (c,d) $\tilde{t}$ = 18.30 for (a,c) strong onshore wind Re* = 2400 and (b,d) strong offshore wind Re* = −1800. The air-water interface is indicated by the black curve.

wave propagation and at $z/h_0 = -2$ the nondimensional wind speed is $\langle \bar{U} \rangle / C \approx -2.4$ (figure 2). Upstream, the airflow is laminar with strongest positive vorticity near the air water interface. In the lee of the solitary wave, the airflow separates with a trail of quasi-regular vortices ejected off of the back face of the wave, that are smaller than that for the onshore wind case (figure 3a). The offshore-wind solitary wave has weaker front face minimum slope $\min(\partial\eta/\partial x) = -0.37$ and weaker maximum rear face slope $|\partial\eta/\partial x| = 0.31$, relative to the onshore wind case. These differences in solitary wave slope between $\mathrm{Re}^* = 2400$ and $\mathrm{Re}^* = -1800$ suggest the wind is at $\tilde{t} = 14.0$ already having an effect on the solitary wave.

Later at $\tilde{t} = 18.30$, the differences between the $\mathrm{Re}^* = 2400$ and $\mathrm{Re}^* = 1800$ solitary wave are even starker. At $\tilde{t} = 18.30$, the $\mathrm{Re}^* = 2400$ solitary wave peak is located at $x_{\mathrm{pk}}/h_0 \approx 39.2$ and has transformed substantially (figure 3c). The overturning jet has just formed as the front face slope goes beyond vertical with maximum $\eta/h_0 = 0.74$ and infinite maximum steepness. The back face, with maximum $|\partial\eta/\partial x| = 0.3$, is even more gently sloped than the back-face at $\tilde{t} = 14.0$. The airflow is laminar upstream of the solitary wave, and the airflow separates on the front face of the wave with recirculating vortices. At $\tilde{t} = 18.30$, the $\mathrm{Re}^* = -1800$ solitary wave is quite different from the $\mathrm{Re}^* = 2400$ solitary wave. The solitary wave peak is located at $x_{\mathrm{pk}}/h_0 = 39.0$ with maximum height $\eta_{\mathrm{pk}}/h_0 = 0.74$ and although the front-face has steepened significantly with maximum steepness of $|\partial\eta/\partial x| = 2.15$, the overturning jet has not yet formed (figure 3d). The back-face maximum slope is much weaker at $|\partial\eta/\partial x| = 0.3$. The upstream airflow is laminar, but the airflow separation near the crest is more intense than at $\tilde{t} = 14.0$ as the wave is steeper and lee vortices continue to be shed. The differences in the shoaling solitary wave for onshore and offshore wind both during shoaling ($\tilde{t} = 14.0$) and the stronger differences at- or near-overturning at ($\tilde{t} = 18.30$) demonstrate wind-effects on solitary wave shoaling.

3.2. *Statistics of solitary wave shoaling under wind*

We next examine statistics of soliton shoaling under wind. As before, η_{pk}/h_0 is the peak of the air-water interface associated with the solitary wave, with horizontal location x_{pk}/h_0. The minimum slope on the front face of the solitary wave is defined as $\min(\partial\eta/\partial x)$. We also examine the nondimensional water energy $\tilde{E}_{\mathrm{w}}$ (2.12). These parameters are estimated from $\tilde{t} = 11$ to $\tilde{t} = 17.9$ corresponding to the time when shoaling on the slope commences to just prior to when the $\mathrm{Re}^* = 2400$ slope goes vertical.

For all cases x_{pk}/h_0 is essentially linear function of $\tilde{t}$ (figure 4a), indicating a constant propagation speed as the solitary wave propagates over the rapidly varying bathymetry. The lack of solitary wave deceleration is similar to other model simulations over rapidly varying bathymetry (Guyenne & Grilli 2006) and observations at the Surf Ranch (Feddersen *et al.* 2023). For both Re^*, a least-squares fit between time and x_{pk}/h_0 yields skill exceeding $r^2 = 0.9996$. For $\mathrm{Re}^* = 2400$, the fit solitary wave speed is $\tilde{C} = 1.33$. For $\mathrm{Re}^* = -1800$, the fit solitary wave speed $\tilde{C} = 1.32$ is slightly slower, indicating that wind has only a small effect on propagation speed. Both fit speeds are slightly larger than the theoretical solitary wave speed of $\tilde{C} = 1.265$. Prior to shoaling, the solitary wave has already adjusted from the initial condition of $a_0/h = 0.6$ to a larger value near $\eta_{\mathrm{pk}}/h_0 \approx 0.68$ for both Re^* (figure 4b). As the solitary wave shoals up the steep slope, η_{pk}/h_0 slowly grows and even close to overturning, η_{pk}/h_0 is still < 0.77. Overall, the solitary wave amplitude shoaling (η_{pk}/a_0) is slightly slower than Green's law $(h/h_0)^{-1/4}$ consistent with the large-slope and significant nonlinearity regime of Knowles & Yeh (2018). The $\mathrm{Re}^* = 2400$ solitary wave does have larger η_{pk}/h_0 during much of shoaling but as the solitary wave steepens significantly near $\tilde{t} = 17.9$, the η_{pk}/h_0 reduces slightly as overturning nears. Similar features can be seen in the simulations of Grilli *et al.* (1997).

The wave energy $\tilde{E}_{\mathrm{w}}$ has small changes during shoaling ($11 < \tilde{t} < 17.9$) between $\mathrm{Re}^* = 2400$ and $\mathrm{Re}^* = -1800$ (figure 4c). At $\tilde{t} = 11$, $\tilde{E}_{\mathrm{w}}$ is slightly (two percent) larger ($\tilde{E}_{\mathrm{w}} = 0.554$) for $\mathrm{Re}^* = 2400$ relative to $\mathrm{Re}^* = -1800$ ($\tilde{E}_{\mathrm{w}} = 0.542$). For $\mathrm{Re}^* = -1800$, $\tilde{E}_{\mathrm{w}}$ decays weakly to

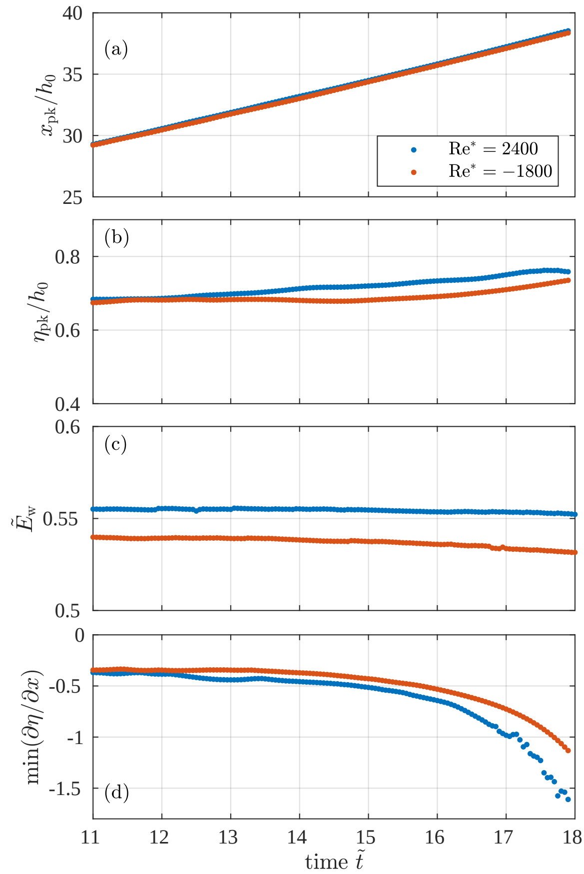

Figure 4. Statistics of solitary wave shoaling under wind versus nondimensional time $\tilde{t}$ for $\mathrm{Re}^* = 2400$ and $\mathrm{Re}^* = -1800$: (a) horizontal location of peak water elevation x_{pk}/h_0, (b) maximum water elevation η_{pk}/h_0, (c) nondimensional water energy $\tilde{E}_{\mathrm{w}}$ (2.11) and (d) minimum air-sea interface slope $\min(\partial\eta/\partial x)$. The time period shown $11 < \tilde{t} < 17.9$ corresponds to solitary wave shoaling on the slope until just prior to the slope going vertical for $\mathrm{Re}^* = 2400$.

$\tilde{E}_{\mathrm{w}} = 0.532$ at $\tilde{t} = 17.9$, reflecting both the offshore wind slowly extracting energy from the solitary wave and small viscous dissipation at the wave Reynolds numer $\mathrm{Re}_{\mathrm{w}} = 4 \times 10^4$. For $\mathrm{Re}^* = 2400$, the wave energy $\tilde{E}_{\mathrm{w}}$ is essentially constant during shoaling with $\tilde{E}_{\mathrm{w}} = 0.553$ at $\tilde{t} = 17.9$, as small onshore wind energy input and weak viscous dissipation largely balance. Overall, for these extreme Re^*, energy transfer between wind and the solitary wave over this short duration of shoaling is weak.

Unlike η_{pk}/h_0 and $\tilde{E}_{\mathrm{w}}$, the minimum slope $\min(\partial\eta/\partial x)$ evolves significantly during shoaling with strong differences between $\mathrm{Re}^* = 2400$ and $\mathrm{Re}^* = -1800$ (figure 4d). At $\tilde{t} = 11$, $\min(\partial\eta/\partial x) \approx -0.36$ for both Re^* with slightly more negative $\min(\partial\eta/\partial x)$ for $\mathrm{Re}^* = 2400$. As discussed in Section 3.1, by $\tilde{t} = 14$, the differences in $\min(\partial\eta/\partial x)$ between the two Re^* have grown substantially with $\min(\partial\eta/\partial x) = -0.46$ for $\mathrm{Re}^* = 2400$ and $\min(\partial\eta/\partial x) = -0.37$ for $\mathrm{Re}^* = -1800$. For both Re^*, $\min(\partial\eta/\partial x)$ continues to evolve rapidly with large differences between Re^* for $\tilde{t} > 15$. For example, by $\tilde{t} = 17.0$ the $\mathrm{Re}^* = 2400$ $\min(\partial\eta/\partial x) = -0.98$ whereas the $\mathrm{Re}^* = -1800$ $\min(\partial\eta/\partial x) = -0.73$ is smaller in magnitude. Shortly thereafter at $\tilde{t} = 17.9$, $\min(\partial\eta/\partial x) = -1.61$

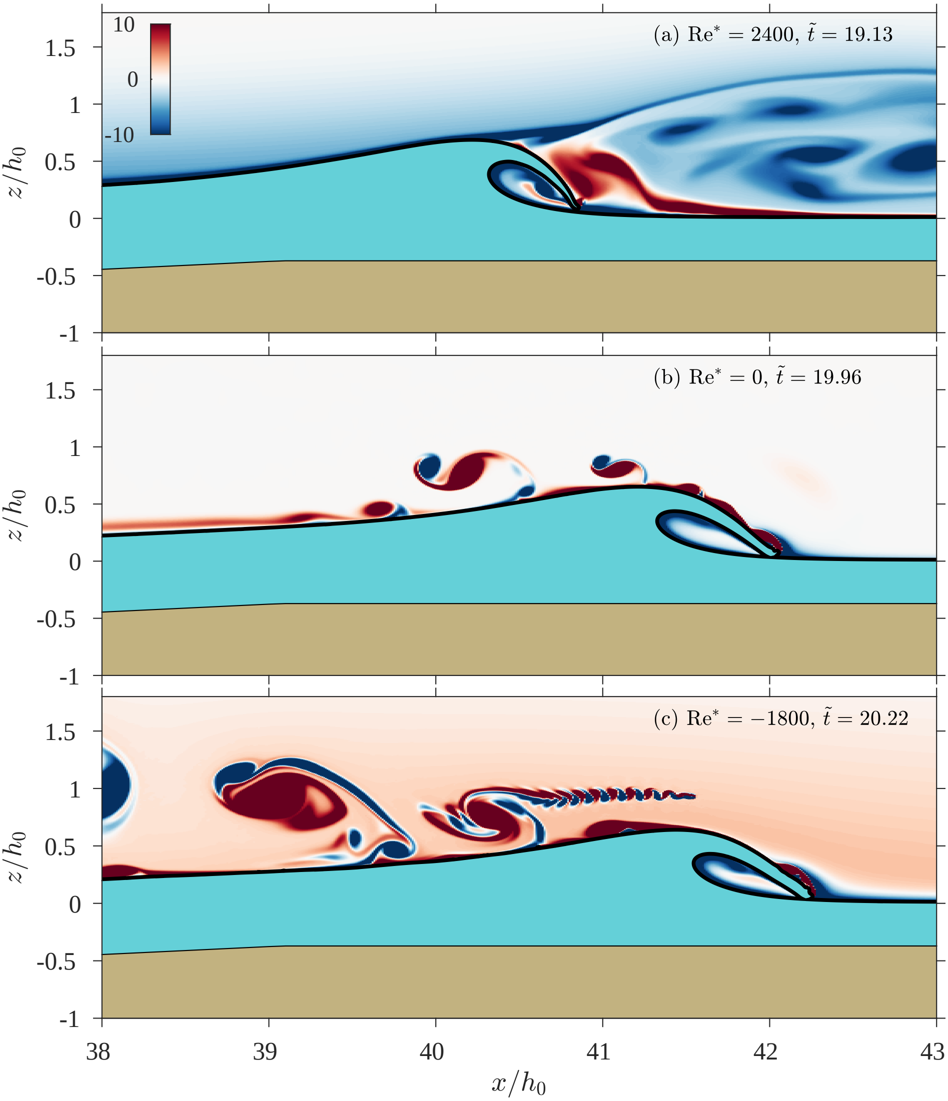

Figure 5. Overturning solitary wave (aqua blue) at the moment of overturning jet impact on the water surface, with the bathymetry (brown) and overlaid air vorticity as a function of horizontal x/h_0 and vertical z/h_0 coordinates: (a) Onshore wind $\mathrm{Re}^* = 2400$ and $\tilde{t} = 19.13$, (b) no wind, $\mathrm{Re}^* = 0$ and $\tilde{t} = 19.96$, and (c) offshore wind $\mathrm{Re}^* = -1800$ and $\tilde{t} = 20.22$. The air-water interface is indicated by the black curve.

and -1.13 for $\mathrm{Re}^* = 2400$ and 1800, respectively, indicating the rapid evolution. These strong differences in $\min(\partial\eta/\partial x)$ for the two Re^* indicate wind effects during shoaling.

3.3. *The moment of overturning jet impact*

We examine the moment in time when the overturning jet impacts the water surface in front of it for three different wind speeds (figure 5). The time of impact is defined as the earliest time at which the vertical separation between the lowest part of the overturning jet and the water surface below it is $\Delta z/h_0 \leqslant 0.015$, or 2.5% of the initial solitary wave amplitude $a_0/h_0 = 0.6$. This is also about $4\times$ the minimum model resolution of $\Delta z/h_0 = 3.7 \times 10^{-3}$ at 14 levels of refinement. With

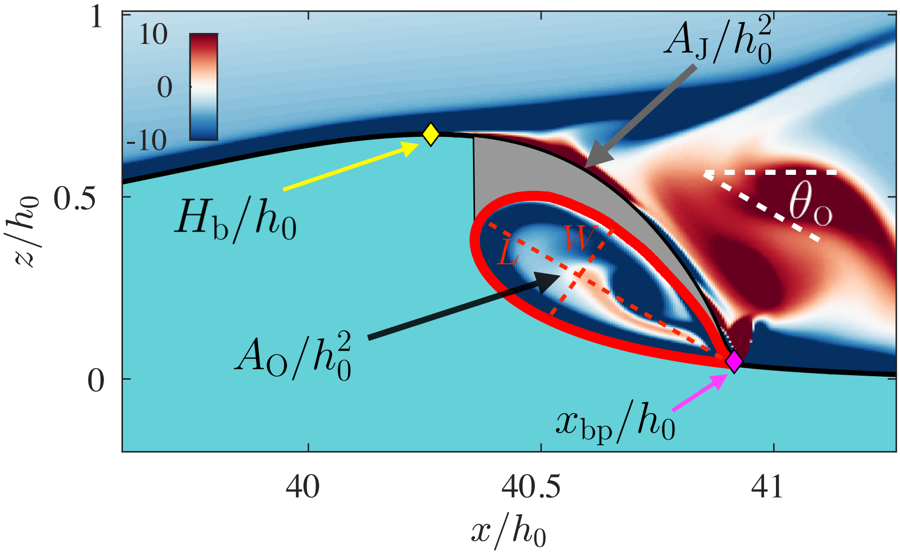

Figure 6. Overturning solitary wave (aqua blue) at the moment of overturning jet impact on the water surface with overlaid air vorticity as a function of horizontal x/h_0 and vertical z/h_0 coordinates for the $\mathrm{Re}^* = 2400$ case and definitions for the geometrical properties of the overturning wave. The air-water interface is represented by the black curve. The magenta diamond indicates the nondimensional breakpoint location x_{bp}/h_0 and the yellow diamond indicates the nondimensional breaking wave height H_{b}/h_0. The red curve indicates the enclosed overturn region with area A_{o}/h_0^2, and the gray region indicates the overturning jet area A_{J}/h_0^2. The dashed red lines schematize the length L and width W of the overturn. The overturn orientation relative to horizontal θ_{o} is indicated.

this time of impact definition, the jet is just about to impact but has not quite yet. The breakpoint location x_{bp}/h_0 is defined as the horizontal location of smallest $\Delta z/h_0$. At the time resolution of model output $\Delta\tilde{t} = 0.01$, occasionally the impact time is chosen when the jet has just made contact with the surface below, and then x_{bp}/h_0 is defined as the smallest location to cross $z/h_0 = 0$. This breakpoint location definition is analogous to that used in Feddersen *et al.* (2023).

For $\mathrm{Re}^* = 2400$, the moment of jet impact occurs at $\tilde{t} = 19.13$ making contact at $x_{\mathrm{bp}}/h_0 = 40.85$ (figure 5a). The overturn has the classical parametric cubic shape (Longuet-Higgins 1982) seen in both models and observations of wave overturning. The $\mathrm{Re}^* = 2400$ overturning jet is relatively thin and the overturn orientation is relatively inclined. For $\mathrm{Re}^* = 0$, overturning-jet impact occurs at $\tilde{t} = 19.96$ at $x_{\mathrm{bp}}/h_0 = 42.05$ (figure 5b), farther onshore and later than for $\mathrm{Re}^* = 2400$. Relative to $\mathrm{Re}^* = 2400$, the $\mathrm{Re}^* = 0$ maximum height of the wave is slightly reduced, the overturning jet is thicker, and the overturn is longer and oriented more horizontal. Although, in the fixed reference frame, the air velocity is essentially zero at $z/h_0 \geqslant 2$ (figure 2), as the solitary wave moves with speed near $\tilde{C}$, the relative air velocity is substantial, and vortices are shed behind the overturning solitary wave. For $\mathrm{Re}^* = -1800$, the overturning jet impact occurs even later at $\tilde{t} = 20.22$ and is located at $x_{\mathrm{bp}}/h_0 = 42.25$ (figure 5c). Relative to $\mathrm{Re}^* = 0$, the $\mathrm{Re}^* = -1800$ has an even thicker overturn jet and a longer overturn, which is oriented even more horizontally. The farther offshore overturning jet-impact with onshore wind ($\mathrm{Re}^* = 2400$) relative to offshore wind ($\mathrm{Re}^* = -1800$) is consistent with laboratory (Douglass 1990) and field scale experiments (Feddersen *et al.* 2023) experiments.

We note in passing that a vortex street is visible in the lee of the overturning wave in figure 5c. This is the wake of a small droplet torn from the crest of the wave during the initial stage of overturning. Such droplets occasionally appear in the simulations we present, but we do not consider them in detail as they do not have great physical significance in our 2D setting, and they do not discernibly affect the evolving breaker.

3.4. *Definition of Geometrical Parameters of Wave Overturning*

Next, we define geometrical parameters of the overturning wave at the moment of jet-impact for the $\mathrm{Re}^* = 2400$ case (figure 6) following the methodology used in the experimental study over wave overturning (Feddersen *et al.* 2023). The first geometrical parameter is the breakpoint location x_{bp}/h_0 (magenta diamond in figure 6). The breaking wave height H_b/h_0 is defined as the maximum elevation of the air-water interface (yellow diamond in figure 6), as no trough is present in front of the solitary wave, i.e., $z/h_0 = 0$ (figure 3, 5). The overturn boundary enclosing the air within the overturn (red curve in figure 6) has area A_o/h_0^2 (figure 6). The region of the overturning jet is the defined as the upper region of water where the air-water interface is multi-valued in x/h_0, with area A_J/h_0^2 (gray region in figure 6). Note, overturning jet area was not measured in previous studies. As done previously for overturn area (O'Dea *et al.* 2021; Feddersen *et al.* 2023), both overturn area and jet area are normalized by H_b/h_0 so that analysis is performed on $A_\mathrm{o}/H_\mathrm{b}^2$ and $A_\mathrm{J}/H_\mathrm{b}^2$. The overturn boundary has shape similar to the functional form (Longuet-Higgins 1982) used previously to fit laboratory and field measured wave overturns (e.g. Blenkinsopp & Chaplin 2008; O'Dea *et al.* 2021; Feddersen *et al.* 2023). Overturn length L and width W (figure 6) are estimated by rotating the overturn boundary by the overturn angle θ_o (figure 5) to the horizontal and fitting to the functional form (Longuet-Higgins 1982)

$$\frac{z'}{W} = \pm\frac{3\sqrt{3}}{4}\sqrt{\frac{x'}{L}}\left(\frac{x'}{L} - 1\right), \tag{3.1}$$

where the x' and z' coordinates are oriented along and across the overturn, and L and W are the overturn length and width (figure 7).

3.5. *Geometrical Parameters dependence on Wind*

Across all Re^*, x_{bp}/h_0 varies from 40.9 to 42.2 with smaller x_{bp}/h_0 (farther offshore) for increasing Re^* as in figure 5. To highlight wind effects, we define a demeaned breakpoint location as

$$\frac{\Delta x_{\mathrm{bp}}}{h_0} = \frac{\langle x_{\mathrm{bp}}\rangle}{h_0} - \frac{x_{\mathrm{bp}}}{h_0}, \tag{3.2}$$

where $\langle\rangle$ is an average over the eight simulations at different Re^*. Thus, positive $\Delta x_{\mathrm{bp}}/h_0$ is farther offshore, consistent with previous experiment work (Douglass 1990; Feddersen *et al.* 2023). From no-wind ($\mathrm{Re}^* = 0$) to onshore wind (positive Re^*), $\Delta x_{\mathrm{bp}}/h_0$ increases rapidly from -0.2 to 0.9, with the largest increase at larger Re^* (figure 7a). From no-wind to offshore wind (negative Re^*), $\Delta x_{\mathrm{bp}}/h_0$ decreases more slowly with Re^* than for onshore wind reaching $\Delta x_{\mathrm{bp}}/h_0 = -0.4$ at $\mathrm{Re}^* = -1800$ (figure 7a). This breakpoint dependence on the wind is qualitatively consistent with experimental results (Douglass 1990; Feddersen *et al.* 2023). Normalizing the field-scale results of Feddersen *et al.* (2023) by h_0 as we do here, yield observed field-scale $\Delta x_{\mathrm{bp}}/h_0$ variation of ± 0.8 consistent with modeled $\Delta x_{\mathrm{bp}}/h_0$ variation. However, the field-scale variation occurs from substantially weaker wind variations than seen in the modeling, as will be discussed. We next examine the effect of wind on the breaking wave height H_b/h_0. For no wind ($\mathrm{Re}^* = 0$), $H_\mathrm{b}/h_0 = 0.64$ and for onshore wind H_b/h_0 increases to $H_\mathrm{b}/h_0 = 0.674$ for $\mathrm{Re}^* = 2400$ (figure 7b). From no wind to offshore wind, the H_b/h_0 decreases slightly to $H_\mathrm{b}/h_0 = 0.627$. Note that this range of H_b/h_0 is a reduction relative to the largest values of η_{pk}/h_0 during shoaling (figure 4b), similar to potential flow simulations of overturning solitary waves (Grilli *et al.* 1997).

We now examine wind effects on nondimensional overturn ara $A_\mathrm{o}/H_\mathrm{b}^2$ (figure 7c). From no-wind ($\mathrm{Re}^* = 0$) to onshore wind, $A_\mathrm{o}/H_\mathrm{b}^2$ decreases from $A_\mathrm{o}/H_\mathrm{b}^2 = 0.352$ at $\mathrm{Re}^* = 0$ to $A_\mathrm{o}/H_\mathrm{b}^2 = 0.301$

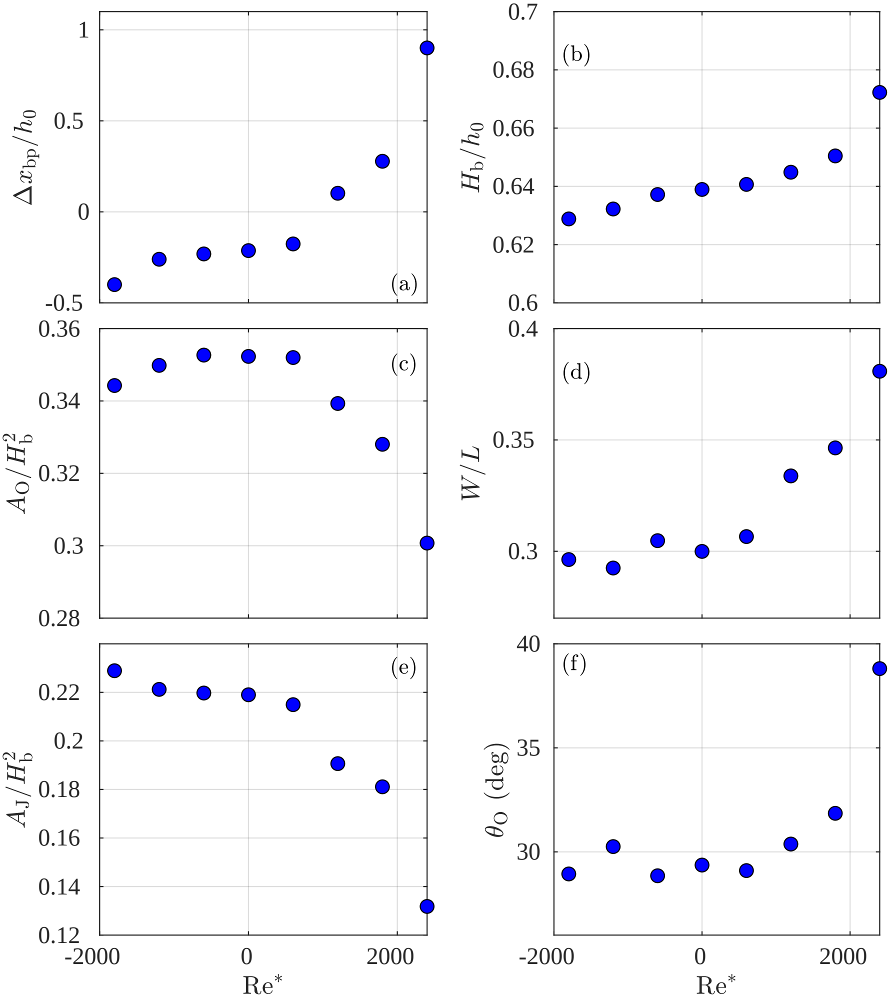

Figure 7. Geometrical parameters of the overturning wave as a function of wind Reynolds number Re*: (a) Demeaned nondimensional breakpoint location $\Delta x_{\mathrm{bp}}/h_0$ (3.2) (b) wave height at breaking H_b/h_0, (c) nondimensional wave overturn area $A_\mathrm{o}/H_\mathrm{b}^2$, (d) overturn aspect ratio W/L, and (e) nondimensional wave jet area $A_\mathrm{J}/H_\mathrm{b}^2$, (f) overturn angle θ_o.

at Re* = 2400. From no-wind to offshore wind, $A_\mathrm{o}/H_\mathrm{b}^2$ is relatively constant before decreasing slightly to $A_\mathrm{o}/H_\mathrm{b}^2 = 0.344$ at Re* $= -1800$. This relationship with $A_\mathrm{o}/H_\mathrm{b}^2$ and Re* is qualitatively consistent with field-scale experiment (Feddersen *et al.* 2023). However, the experimental $A_\mathrm{o}/H_\mathrm{b}^2$ varied between 0.2 and 0.4, a larger variation than seen in the model, for weaker wind or Re* variation. Next, we examine the overturn aspect ratio W/L (figure 7d). For no-wind, $W/L = 0.300$ and increases for onshore wind to $W/L = 0.381$ at Re* = 2400. For offshore wind, W/L is largely constant varying from 0.296 to 0.305. This pattern of increasing W/L with positive Re* is inconsistent with the experimental results of Feddersen *et al.* (2023), who found W/L decreased with increasing onshore wind. Furthermore, the experimental results had larger W/L range, varying from 0.3 to 0.5, larger than the 0.3 to 0.38 modeled variation in W/L.

We next examine the wind effect on the non-dimensional jet area $A_\mathrm{J}/H_\mathrm{b}^2$ (figure 7e). For no-wind,

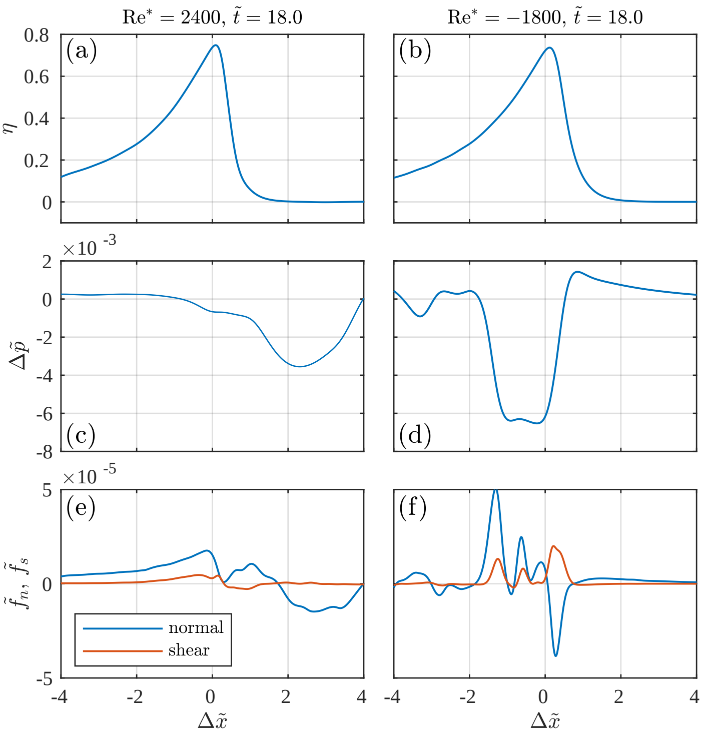

Figure 8. Snapshots at $\tilde{t}$ = 18.0 of (top) $\tilde{\eta}$, (middle) $\Delta\tilde{p}$, and (bottom) viscous normal $\tilde{f}_n$ and shear $\tilde{f}_s$ stresses versus $\Delta\tilde{x}$ for (left) $\mathrm{Re}^* = 2400$ and (right) $\mathrm{Re}^* = -1800$.

$A_\mathrm{J}/H_\mathrm{b}^2 = 0.219$, which decreases rapidly with onshore wind to $A_\mathrm{J}/H_\mathrm{b}^2 = 0.132$ for $\mathrm{Re}^* = 2400$. For offshore wind, $A_\mathrm{J}/H_\mathrm{b}^2$ is largely constant with Re^*, varying from 0.229 to 0.219. Overturn jet area has not been previously examined experimentally or numerically. Lastly, we examine the overturn angle θ_o (figure 7f). For $\mathrm{Re}^* = 0$, the overturn angle $\theta_\mathrm{o} = 29°$ and this increases with onshore wind to $\theta_\mathrm{o} = 39°$ for $\mathrm{Re}^* = 2400$, consistent with the orientations of the overturn seen in figure 5a,b. For offshore wind, θ_o varies only weakly with negative Re^*. This range of θ_o is smaller than the $\theta_\mathrm{o} \approx 42° \pm 8°$ at the Surf Ranch (Feddersen *et al.* 2023). It is also on the low end of $30° < \theta_\mathrm{o} < 60°$ reported in surfzone overturning waves (O'Dea *et al.* 2021).

3.6. *Relative strength of pressure and shear stress*

Airflow can affect the water-based solitary wave via two mechanisms on the air-water interface. The first mechanism is through an air-flow induced pressure, and the second mechanism either normal or shear viscous stresses. Here we will examine the relative strength of pressure and viscous stresses on the air-water interface at a shoaling time just prior to when η goes multivalued. Henceforth, we will use nondimensional variables indicated with a $\tilde{()}$. As discussed in Section 2.1.6, air pressure and velocity gradients are output and estimated at a small nondimensional distance $\Delta = 0.01$ normal to the air-water interface. This prevents biases in pressure estimation due to noise in air-water interface curvature estimates. From the velocity gradients, the nondimensional viscous stress tensor $\tilde{\boldsymbol{S}}$ (in index notation)

$$\tilde{S}_{ij} = \tilde{\mu}_a \left(\frac{\partial \tilde{u}_i}{\partial \tilde{x}_j} + \frac{\partial \tilde{u}_j}{\partial \tilde{x}_i} \right) \tag{3.3}$$

where the nondimensional air dynamic viscosity is $\tilde{\mu}_a = \mathrm{Re}_\mathrm{w}^{-1}\mu_\mathrm{a}/\mu_\mathrm{w} = 4.53 \times 10^{-7}$. The normal ($\tilde{\mathbf{n}}$) and parallel ($\tilde{\mathbf{s}}$) unit vectors to the air-water interface are also estimated. At the air-water interface η, the viscous normal stress is $\tilde{f}_n = \tilde{\mathbf{n}} \cdot \tilde{\boldsymbol{S}} \cdot \tilde{\mathbf{n}}$ and the viscous shear stress is $\tilde{f}_s = \tilde{\mathbf{s}} \cdot \tilde{\boldsymbol{S}} \cdot \tilde{\mathbf{n}}$. To isolate the pressure disturbance associated with the solitary wave, the air-water interface nondimensional pressure differential $\Delta\tilde{p}$ is estimated as the pressure $\tilde{p}$ minus an upstream pressure located at $\Delta\tilde{x} = \pm 6$ depending on the wind direction.

We examine the end of the shoaling period at $\tilde{t} = 18.0$, where the $\mathrm{Re}^* = 2400$ air-water interface $\tilde{\eta}$ is close to being multivalued. For both $\mathrm{Re}^* = 2400$ and $\mathrm{Re}^* = -1800$ the $\tilde{\eta}(\Delta\tilde{x})$ profile have classic sawtooth shapes with steep front face and a milder-sloped back face (figure 8a,b), with steeper front face for $\mathrm{Re}^* = 2400$ (e.g. figure 4d). For $\mathrm{Re}^* = 2400$, the windward side of the solitary wave ($-3 < \Delta\tilde{x} < -1$ has mildly elevated $\tilde{p} \approx 0.2 \times 10^{-3}$ (figure 8c) and on the leeward side (in front of the wave) a deep low pressure with minimum $\tilde{p} = -3.7 \times 10^{-3}$ occurs over $0 < \Delta\tilde{x} < 4$. This low pressure is associated with the strongly separated flow that occurs many $\Delta\tilde{x}$ in front of the wave (figure 3a,b). In contrast, the $\mathrm{Re}^* = -1800$ simulation has much higher $\tilde{p} \approx 1.5 \times 10^{-3}$ on the windward wave face and a deeper low pressure with minimum $\tilde{p} = -6.3 \times 10^{-3}$ in the lee of the wave (figure 8d). For $\mathrm{Re}^* = -1800$, the lee low-pressure width ($\approx 2\Delta\tilde{x}$ wide) is half as wide as that for $\mathrm{Re}^* = 2400$ due to the differences flow separation and attachment. On the air-sea interface, the magnitude of the viscous stresses relative to pressure are generally small (figure 8e,f). For $\mathrm{Re}^* = 2400$ and $\mathrm{Re}^* = -1800$, both normal and shear stresses have magnitude $< 5 \times 10^{-5}$, roughly a factor of 100× smaller than that of $\tilde{p}$. The normal stresses are a factor of 2-3× larger than the shear stresses for both $\mathrm{Re}^* = 2400$ and $\mathrm{Re}^* = -1800$. The $\mathrm{Re}^* = -1800$ viscous stresses are larger than those of $\mathrm{Re}^* = 2400$ due to the stronger shear between the wind blowing counter to the $+\Delta\tilde{x}$ directed solitary wave velocities.

This demonstrates that the pressure forces must be those that are influencing changes in wave shoaling and overturning. This result at $\tilde{t} = 18.0$ is consistent at other wave shoaling times $11 < \tilde{t} < 18$ where pressure variability exceeds viscous stresses by 100×. These results are consistent with DNS simulations of wind-wave growth which found pressure about 10× larger than viscous stresses (Wu *et al.* 2022). They also found that pressure forces grew with wave slope particularly for smaller wave age, but that viscous forces did not grow. During shoaling, the soliton is steeper (4d) than any regime of Wu *et al.* (2022). Moreover, Wu *et al.* (2022) investigated a lower Re^*, for which viscous forces are likely to be stronger relative to inertial effects than for the strongest Re^* presented here. These observations may explain why our ratio of pressure to viscous forces is so strong relative to Wu *et al.* (2022).

3.7. *The Surface Dynamic Boundary Condition*

With the viscous stresses negligible, we next examine the role of $\tilde{p}$ on the air-water interface $\tilde{\eta}$ using the irrotational flow surface dynamic boundary condition boosted into a moving horizontal reference frame $\Delta\tilde{x}$ with constant best-fit speed $\tilde{C}$ (figure 4a) for the $\mathrm{Re}^* = 2400$ and $\mathrm{Re}^* = -1800$ cases. In the $\Delta\tilde{x}$ reference frame moving with constant speed $\tilde{C}$, the nondimensional dynamic boundary condition is transformed to

$$\frac{\partial\tilde{\phi}}{\partial\tilde{t}} - \tilde{C}\tilde{u} + \frac{1}{2}\left[\tilde{u}^2 + \tilde{w}^2\right] + \tilde{\eta} + \Delta\tilde{p} = \tilde{T} \tag{3.4}$$

where $\tilde{\phi}$ is the nondimensional velocity potential, all terms are evaluated at $\tilde{z} = \tilde{\eta}$, $\Delta\tilde{p}$ is the pressure jump at the surface, and $\tilde{T}$ represents the nondimensional surface tension term, for which the curvature κ from (2.1)can be written in terms of the (single-valued) interface $\tilde{\eta}$

$$\tilde{T} = \mathrm{Bo}^{-1}\,\frac{\partial^2\tilde{\eta}/\partial(\Delta\tilde{x})^2}{\left(1 + (\partial\tilde{\eta}/\partial(\Delta\tilde{x}))^2\right)^{3/2}}. \tag{3.5}$$

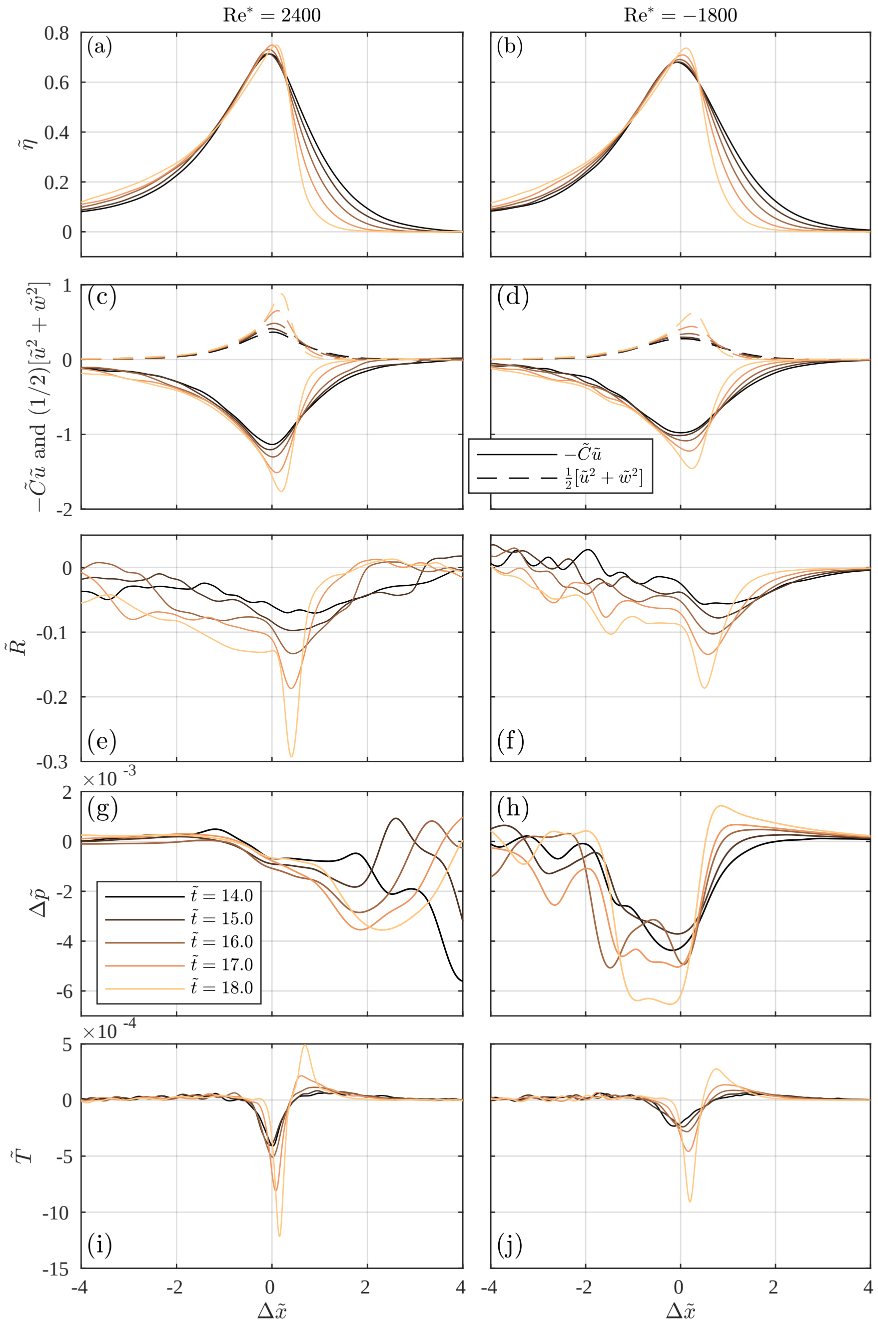

Figure 9. Surface dynamic boundary condition terms (3.4) versus $\Delta\tilde{x}$ for (left) $\mathrm{Re}^* = 2400$ and (right) $\mathrm{Re}^* = -1800$ and from time $\tilde{t} = 14.0$ (black) to $\tilde{t} = 18.0$ (gold) at $\Delta\tilde{t} = 1$: (a,b) $\tilde{\eta}$, (c,d) $-\tilde{C}\tilde{u}$ (solid) and $(1/2)[\tilde{u}^2 + \tilde{w}^2]$ (dashed), (e,f) the residual term $\tilde{R}$ (3.6), (g,h) $\Delta\tilde{p}$, and (i,j) the surface tension term $\tilde{T}$ (3.5).

The change in the solitary wave in the moving reference frame is represented by $\partial\tilde{\phi}/\partial\tilde{t}$, and for an unchanging solitary wave propagating at $\tilde{C}$, $\partial\tilde{\phi}/\partial\tilde{t} = 0$. Thus, for $\Delta\tilde{p} = 0$ and no surface tension, the residual

$$\tilde{R} = -\tilde{C}\tilde{u} + \frac{1}{2}\left[\tilde{u}^2 + \tilde{w}^2\right] + \tilde{\eta} \tag{3.6}$$

is zero for an unchanging solitary wave. Nonzero $\tilde{R}$ can therefore be interpreted as the signature of the wave's unsteady evolution i.e. of its evolving asymmetry and nonlinear steepening. The terms $-\tilde{C}\tilde{u}$, $(1/2)[\tilde{u}^2 + \tilde{w}^2]$, and $\tilde{T}$ also are evaluated on the air-water interface. The terms of (3.4) are analyzed during the latter part of the shoaling phase ($14 \leqslant \tilde{t} \leqslant 18$) when significant differences in the minimum slope on the front of the wave face occur (figure 4d) and when $\tilde{\eta}$ is still single-valued.

During shoaling ($\tilde{t} = 14.0$ to $\tilde{t} = 18.0$), both $\mathrm{Re}^* = 2400$ and $\mathrm{Re}^* = -1800$ solitary waves evolve from a more symmetrical wave to an asymmetrical sawtooth type pattern (figure 9a,b) as maximum $\tilde{\eta} \approx 0.7$ throughout (as in figure 4a). Although subtle differences between the $\mathrm{Re}^* = 2400$ and $\mathrm{Re}^* = -1800$ solitary waves are evident at $\tilde{t} = 14.0$, by $\tilde{t} = 18.0$, the $\mathrm{Re}^* = 2400$ solitary wave front face is clearly significantly steeper than for $\mathrm{Re}^* = -1800$, consistent with figure 4d. For both Re^*, the peak $-\tilde{C}\tilde{u} \approx -1$ at $\tilde{t} = 14.0$ which grows in time and becomes more asymmetric (solid, figure 9c,d), with $\mathrm{Re}^* = 2400$ having more growth and asymmetry at $\tilde{t} = 18.0$. For both Re^* at $\tilde{t} = 14.0$, the nonlinear term $(1/2)[\tilde{u}^2 + \tilde{w}^2]$ is largely symmetric with maximum of 0.36 and 0.27 for $\mathrm{Re}^* = 2400$ and $\mathrm{Re}^* = -1800$, respectively (dashed, figure 9c,d), indicating wind-induced difference in shoaling at this time. This also indicates that the weakly nonlinear assumption is starting to be questionable. With increasing time, $(1/2)[\tilde{u}^2 + \tilde{w}^2]$ increases dramatically to values of 0.88 and 0.63 at $\tilde{t} = 18.0$ and also becomes asymmetric, indicating strong nonlinearity at this time, particularly for $\mathrm{Re}^* = 2400$.

Although the $\tilde{\eta}$, $-\tilde{C}\tilde{u}$, and $(1/2)[\tilde{u}^2 + \tilde{w}^2]$ terms are $O(1)$ (figure 9a-d), the residual term $\tilde{R}$, that sums these terms, is an order of magnitude smaller (figure 9g,h). At $\tilde{t} = 14.0$, R has a minimum of ≈ -0.06 that is slightly more negative and broader for $\mathrm{Re}^* = 2400$. Although over time $\tilde{R}$ grows broadly in $\Delta\tilde{x}$, for $\tilde{t} \geqslant 16.0$, $\tilde{R}$ growth is concentrated at the solitary wave's front face ($0 \leqslant \Delta\tilde{x} \leqslant 0.7$), which attains minimum value of -0.26 and -0.18 for $\mathrm{Re}^* = 2400$ and $\mathrm{Re}^* = -1800$, respectively. This focussed large $\tilde{R}$ leads to rapid $\tilde{\phi}$ changes leading to overturning.

We have already seen the magnitude of pressure term at $\tilde{t} = 18.0$ is $\Delta\tilde{p} \approx 5 \times 10^{-3}$ (figure 8c,d). Over time from $14.0 \leqslant \tilde{t} \leqslant 18.0$, the $\mathrm{Re}^* = 2400$ $\Delta\tilde{p}$ is negative in the lee of the solitary wave ($0 < \Delta\tilde{x} < 2$) and grows with time (figure 9g). In the lee-region but away from the concentrated $\tilde{R}$ ($1 < \Delta\tilde{x} < 2$), $\Delta\tilde{p}$ can be 10% or more of $\tilde{R}$ with the same sign, thus enhancing $\tilde{R}$. From $14.0 \leqslant \tilde{t} \leqslant 18.0$, the $\mathrm{Re}^* = -1800$ $\Delta\tilde{p}$ is also negative in the solitary wave lee ($-1.5 \leqslant \Delta\tilde{x} \leqslant 0$) and grows with time. In this region $\Delta\tilde{p}$ can also be 10% of $\tilde{R}$, but on the rear-face of the soliton. Closer to the time of overturning in the narrow region from $0 \leqslant \Delta\tilde{x} \leqslant 0.7$ where $\tilde{R}$ is concentrated, $\Delta\tilde{p}$ is small (1–2%) relative to $\tilde{R}$. However, the significant $\Delta\tilde{p}$ ($\approx$ 10% of R) in the lee outside of the concentrated region will, during shoaling, induce slowly growing wind-induced differences in wave shape that manifest themselves forward in time until the overturning jet impacts.

As our $\mathrm{Bo} = 4000$ is not at field scale, we also examine the surface tension term $\tilde{T}$ (figure 9i,j). For $\tilde{t} \leqslant 16.0$, the $\tilde{T}$ term is concentrated near $\Delta\tilde{x} = 0$ and is an order of magnitude smaller than $\Delta\tilde{p}$. However, $\tilde{T}$ grows rapidly at the later stages of shoaling and by $\tilde{t} = 18.0$, is $\approx 10^{-3}$ at $\Delta\tilde{x} \approx 0$, still small overall relative to $\Delta\tilde{p}$ in the lee, but of the same magnitude as $\Delta\tilde{p}$ at $\Delta\tilde{x} \approx 0$ for $\mathrm{Re}^* = 2400$ (figure 9i,j). Thus, surface tension effects are generally small but not negligible relative to pressure. Relative to the residual $\tilde{R}$, because $\tilde{T}$ is concentrated where $\tilde{R}$ is concentrated, the surface tension term is orders of magnitude smaller than $\tilde{R}$ for $\tilde{t} \leqslant 18.0$. As the overturning jet forms and falls, then surface tension effects will become even more important.

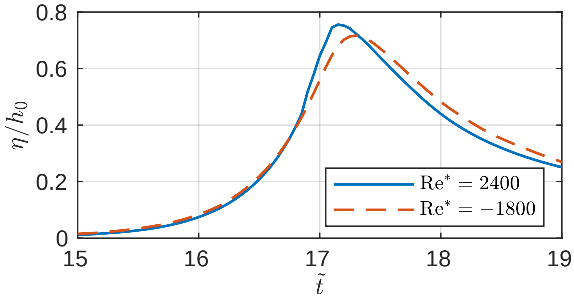

Figure 10. Air-water interface height η/h_0 versus $\tilde{t}$ at location $x/h_0 = 37.5$ for $\mathrm{Re}^* = 2400$ and $\mathrm{Re}^* = -1800$.

4. Discussion of wind effects on the solitary wave

4.1. *Wave shoaling*

We now discuss the wind effects on wave shoaling statistics (figure 4) in the context of previous studies. Zdyrski & Feddersen (2022) derived a vKdV-Burgers equation for soliton shoaling over mildy sloping bathymetry with Jeffrey's style wind forcing (Jeffreys 1925) where the air-water interface pressure is proportional to $\partial\eta/\partial x$. This equation only applies asymptotically well before wave overturning. Although their slope was 3–7× gentler than that here, for offshore to onshore wind, their wind-forced solitary wave had qualitatively similar shoaling to those those here, particularly the steepness of the front of the wave (figure 4d). This similarity occurs even though the air-water interface pressure distribution only has a loose qualitative resemblance to the Jeffrey's style wind forcing. The effect of wind on the solitary wave during shoaling is also qualitatively similar to the laboratory experiments with periodic waves and wind with U/C varying from 0 to 6 (Feddersen & Veron 2005). At a fixed location, the time evolution of the shoaling wave revealed a larger maximum elevation and a temporally-narrower wave than for no wind. Similar features were seen in the solutions of Zdyrski & Feddersen (2022) for onshore and offshore wind. Here, we examine the temporal evolution of η/h_0 at a location of $x/h_0 = 37.5$ that is still on the bathymetric slope but that has shallowed significantly (figure 10). At this virtual wave gauge, the solitary wave has shoaled significantly. At this location, the $\mathrm{Re}^* = 2400$ solitary wave reaches a maximum $\eta/h_0 = 0.76$ at $\tilde{t} = 17.15$ and decays rapidly (blue curve in Figure 10). The $\mathrm{Re}^* = -1800$ solitary wave initially increases similarly to the $\mathrm{Re}^* = 2400$ until $\eta/h_0 = 0.4$ (orange dashed in figure 10). The subsequent maximum $\eta/h_0 = 0.73$ is smaller and shifted slightly later in time. The subsequent temporal decay is also shifted later such that the temporal width of the solitary wave is wider for $\mathrm{Re}^* = -1800$. This is qualitatively similar to the laboratory experiments (Feddersen & Veron 2005) and that of the relatively simple vKdV-Burgers equation (Zdyrski & Feddersen 2022) even accounting for differences in wind forcing, bathymetry, and periodic versus solitary waves.

4.2. *Wave overturning*

The integrated wind-induced surface pressure effect on the shoaling solitary wave then leads to differences in the breakpoint location and the overturn geometrical parameters (figures 6,7). The geometrical parameters in the present numerical simulations have similarities and differences to the field-scale experiment of Feddersen *et al.* (2023). The breakpoint location $\Delta x/h_0$ and overturn area A_o/H_b^2 (figure 7a,c) have similar functional dependence on wind to the field-scale observations. However, the aspect ratio W/L (figure 7d) did not. Furthermore, variation in overturn geometrical parameters require a stronger wind in the present simulations than in the field-scale observations. Here we explore potential causes for these differences.

4.2.1. *Wave Reynolds number and Bond number effects*

The $\mathrm{Re_w} = 4 \times 10^4$ and $\mathrm{Bo} = 4000$ values in this study are much smaller than the field-scale values ($\mathrm{Re_w} = 1.4 \times 10^7$ and $\mathrm{Bo} = 3.6 \times 10^5$) of Feddersen *et al.* (2023) as both $\mathrm{Re_w}$ and Bo are defined in terms of the offshore depth h_0. The wave energy decreases noticeably, particularly for offshore wind, decreasing 2% from $\tilde{t} = 11$ to 18 for $\mathrm{Re}^* = -1800$ (Figure 4c). This decrease is likely due to viscous dissipation at the bottom and air-water interface boundary layers. The boundary layers have thicknesses proportional to $\mathrm{Re_w}^{-1/2}$ (Batchelor 1967) which result in an exponential wave height decrease with decay constant also proportional to $\mathrm{Re_w}^{-1/2}$ (Keulegan 1948). The present $\mathrm{Re_w}$ being much smaller than field values results in more dissipation in the shoaling wave prior to breaking. This may then indirectly require a stronger $\langle U \rangle / C$ than in the field in order to generate the same geometrical overturn parameters.

Any Bo effects are strongest at overturning when interface curvature is largest. For deep-water breaking Stokes waves, Mostert *et al.* (2022) observed that Bo did not affect the nonlinear steepening processes, but directly modulated the geometrical overturn parameters. That study did identify a sufficiently large Bo (defined according to the deep-water breaker wavelength, hence different from the definition here) for which surface tension effects ceased to affect the overturn. That the surface tension contribution reaches the same order as pressure contribution in the surface dynamic boundary condition (Figure 9i,j), implies that surface tension effects are not negligible during overturning, and therefore could have some effect on the overturn geometry, potentially explaining the different aspect ratio relationship to wind between the present simulations and the field experiment. Quantifying potential $\mathrm{Re_w}$ and Bo effects is left for future work.

4.2.2. *Two dimensional versus three dimensional turbulence*

Two-dimensional simulations are convenient with lower computational cost. They provide a good indication of energetic dissipation during wave breaking, as discussed by Iafrati (2009); Deike *et al.* (2015); Mostert *et al.* (2022) in the context of deep water breakers. However, here we are concerned with the wind-induced effects on steepening and overturning solitary wave, which depends on the structure of the airflow over the air-water interface. An obvious 2D effect in the present simulations is the formation of relatively large, wake vortices for both onshore and offshore wind (Figures 3, 5). This air turbulence is constrained to be 2D and and therefore characterized by an inverse energy cascade transferring energy from smaller to larger scales. This is in contrast to the 3D turbulent airflow in the field-scale experiment of Feddersen *et al.* (2023), featuring a direct cascade where larger eddies rapidly break up to smaller scales. The air-flow separation, wake, and reattachment to the solitary wave during wave shoaling would be different between 2D and 3D turbulence, and certainly result in different pressure forcing at the air-water interface. More concretely, for strong onshore wind ($\mathrm{Re}^* = 2400$, figure 3a,c), the airflow wake has scales of the solitary wave height, and flow reattachment occurs many x/h_0 in front of the wave. This results in a wake low pressure that is much broader than for offshore wind (figure 9g,h). If the turbulent were 3D, flow reattachment would likely occur closer to the wave with the wake low pressure region being thus narrower, and particularly for onshore wind, affecting more the wave face. As overturning begins, the wake structure would also be different. With the associated different air-water interface pressure, the resulting overturn geometry would likely be different. This may explain the qualitatively different W/L dependence on wind between simulations (figure 6d) and field experiment as well as simulations requiring a stronger $\langle \bar{U} \rangle / C$.

4.2.3. *Two versus three dimensional wave overturning*

The present simulations and the field study of Feddersen *et al.* (2023) have underlying geometrical differences in wave overturning. In our simulations, the wave overturn is 2D (e.g. figure 5) which can be interpreted as an overturn with infinitely long crest, the entirety of which is simultaneously

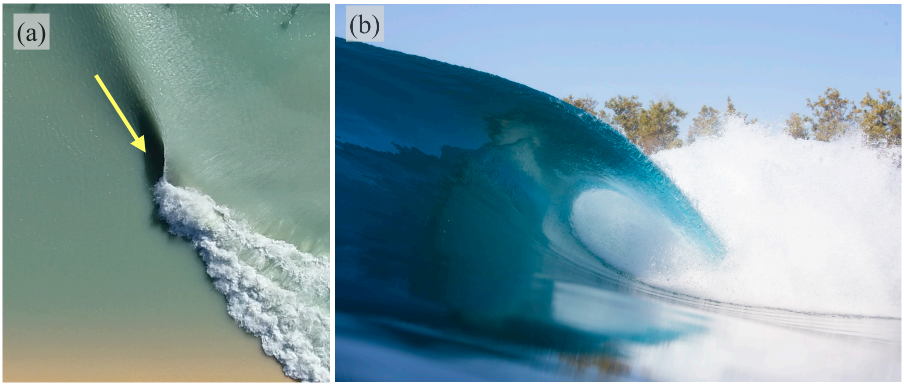

Figure 11. Photos of progressively shoaling and overturning solitary waves at the Surf Ranch: (a) Aerial photo of the obliquely incident solitary wave with arrow indicating a view into the overturn and (b) photo looking into the progressively overturning solitary wave. Note the two photos are of different waves. Progressively overturning waves are the norm in the ocean. Photo credits: (a) Rob Grenzeback, (b) Pat Stacey.

overturning. However, the solitary wave at the Surf Ranch (Feddersen *et al.* 2023) approaches shore obliquely and overturns progressively (figure 11) such that wave overturning is 3D, with significant along-crest variation. The wave transitions along-crest from an offshore region where η is single valued, through the process of overturning, ending in a region where the overturn void collapses and only foam is present (figure 11). Most depth-limited wave breaking in the ocean is 3D. The geometrical differences between 2D and 3D overturning likely result in different pressure distributions during overturning. For a 2D overturn, the moment of impact leads to a dramatic increase in air pressure ($\tilde{p} = 0.08$) trapped by the water of the overturn (figure 12), This $\tilde{p}$ magnitude is 20× to 40× larger than that during shoaling (figure 9). In contrast, a progressive 3D overturn (as in Feddersen *et al.* 2023) always has an overturn volume open to one spanwise side, inducing a spanwise airflow out of the overturn. This would lead to a pressure drop within the overturn, which is not captured in our 2D simulations. The resulting air-water pressure distribution would be different during the overturning. This may explain the differences seen between the 3D overturning (Feddersen *et al.* 2023) and the simulated 2D overturning, particularly in the aspect ratio W/L.

4.3. *Implications and the overturning jet*

The implications of the wind effects on overturned shoaling and overturning waves was discussed in Feddersen *et al.* (2023). Essentially onshore and offshore wind for the otherwise identical wave field will induce changes to wave overturning shape generating different cross-shore wave dissipation patterns, turbulence injection, and sediment suspension. Such effects are not accounted for in modern coastal engineering wave models. Such wind-induced effects, may then eventually affect nearshore morphological evolution. Potential wind effects on turbulence injection can be concretely seen in the modeled overturning jet area $A_\mathrm{J}/H_\mathrm{b}^2$ (figure 7e), whose wind effects have not been examined previously. Spanning the strongest offshore to onshore wind, $A_\mathrm{J}/H_\mathrm{b}^2$ varies by a factor of two, the strongest variation in all the parameters. This $A_\mathrm{J}/H_\mathrm{b}^2$ variation also equates to a large variations in potential energy available in the overturn. This will lead to stronger turbulence injection and increased sediment suspension near the breakpoint for offshore wind relative to onshore wind. Such wind-effects are commonly understood in the surfing community.

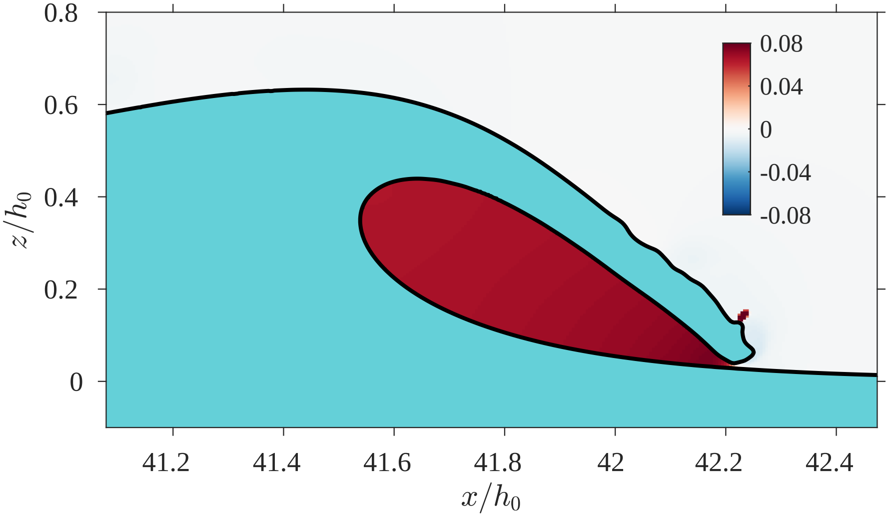

Figure 12. For Re* = −1800 at $\tilde{t}$ = 20.22, overturning solitary wave (aqua blue) at the moment of overturning jet impact on the water surface with overlaid air pressure as a function of horizontal x/h_0 and vertical z/h_0 coordinates. The air-water interface is indicated by the black curve. Note the very high pressure within the nearly enclosed overturn.

5. Summary

Here wind effects (given by the wind Reynolds number Re*) on solitary wave shoaling and overturning were studied with the 2-phase DNS model Basilisk run in two-dimensions. The fixed bathymetry was similar to that of the Surf Ranch. Wave Reynolds and Bond numbers (Re$_\mathrm{w}$ = 4×10^4, Bo = 4000) were fixed, at values orders of magnitude smaller than experiment. A precursor wind-only simulation provides wind initial condition. During the subsequent 2-phase simulations, wind forcing is removed but the wind does not have sufficient time to meaningfully decelerate. The propagating solitary wave sheds a 2D turbulent air wake either in front of the wave for onshore wind or on the back of the wave for offshore wind. The onshore and offshore wind cases have different wake structure. The propagating solitary wave has nearly uniform speed over the rapidly varying bathymetry for all Re*. The solitary wave face slope is clearly influenced by the wind, with steeper slope for stronger onshore wind. Changes to shoaling solitary wave shape are qualitatively consistent with previous laboratory studies and reduced order models. At the moment of overturning jet impact, wind-dependent differences in overturn wave shape are evident and these shapes are quantified by geometrical parameters. The nondimensional breakpoint location and overturn area have similar functional dependence on wind as in experiment. However, modeled wind speeds that are a factor 2–3 stronger than observed are required. The overturn aspect ratio had opposite functional dependence on wind than in experiment. The overturning jet area, not having been previously studied, depends strongly on wind. Airflow can affect the water-based solitary wave through two mechanisms on the air-water interface: pressure or viscous stresses. Throughout the shoaling processes normal and shear viscous stresses are negligible relative to pressure on the air-water interface. Surface tension effects are negligible early in shoaling, but as the wave steepens these effects grow rapidly such that near overturning, surface tension effects are no longer negligible and likely become important in overturning. In a propagating solitary wave frame of reference, pressure is low in the lee and contributes 2-5% to the velocity potential rate of change in the surface dynamic boundary condition. Integrated over the time of shoaling, this leads to changes in the wave shape. Three potential reasons why the modeled overturn aspect ratio differs from experiment and why a stronger modeled wind is required are explored. The first involves potential scale effects resulting from our far smaller $\mathrm{Re_w}$ and Bo than experiment. The second is that the airflow is 2D not 3D, resulting in different flow separation, wake structure, and reattachment than experiment. The third is an underlying difference in the modeled 2D geometry of wave breaking relative to the 3D geometry at the Surf Ranch. The dramatic wind-effects on the nondimensional overturning jet area, and thus to the potential energy available in the overturn, make concrete the implications of wind-induced changes to wave shape.

Acknowledgments We are grateful to the Mark Walk Wolfinger Surfzone Processes Research Fund who provided support to make this research possible. We thank the World Surf League and the Kelly Slater Wave Company for their support of this work. Discussions with Chris Blenkinsopp, Marc Buckley, and Mark McAllister provided useful insight.

Funding. The Mark Walk Wolfinger Surfzone Processes Research Fund supported this research at Scripps Institution of Oceanography.

Declaration of Interests. The authors report no conflict of interest.

Data Availability Statement. Sample Basilisk code used to generate the data in this study can be found at http://basilisk.fr/sandbox/wmostert/windshoaling.c.

Author ORCID. Falk Feddersen, https://orcid.org/0000-0002-5488-9074; Kentaro Hanson, https://orcid.org/0000-0002-0468-226X; Wouter Mostert, https://orcid.org/0000-0001-6251-4136;

Appendix A. Precursor simulations to obtain wind air initial condition

An air-only simulation over a moving solitary wave solid boundary is performed as a precursor to the coupled simulation, providing air initial conditions to the coupled model. The precursor simulation is done under a Galilean transformation in the reference frame of the solitary wave, and is physically equivalent to allowing an unchanging solitary wave to propagate in an arbitrarily long channel of constant depth in the presence of wind. At the solitary wave surface, a no-slip velocity boundary condition given by (2.4) and translated through a Galilean transformation into the solitary wave's frame of reference moving at $\tilde{C}$ in the $+x$ direction is applied. In the solitary wave reference frame, air-flow at the air-water interface must be in the $-x$ direction to match the solitary wave surface velocity boundary conditions (2.4). An external, spatially, and temporally uniform pressure gradient is used to force the wind given by (2.8). The precursor simulation is run until equilibrium. The equilibrium airflow is relatively insensitive to the choice of initial condition, which affects only the time to equilibrate. Here, the initial condition for air vertical velocity is $w = 0$. The initial condition for horizontal velocity is uniform in x and u is set to a logarithmic profile transformed into the solitary wave reference frame with an inner-layer velocity profile that goes to $u = -C$ at the boundary. This u initial condition does not match the no-slip boundary condition on the solitary wave (2.4). However any generated transients are advected way, eventually leaving an equilibrated state for use as initial condition in the coupled air-water simulations. Identical to the coupled simulation, Neumann pressure condition $\partial p/\partial x = 0$ is placed on the inlet and a Dirichlet pressure condition $p = 0$ is placed on the outlet, both uniformly in the vertical. In the moving reference frame, the air-flow in the precursor stage may not be unidirectional, particularly for strong onshore winds as the near-surface airflow will be in the $-x$ direction and higher in the air column will be in the $+x$ direction and thus neither boundary is fully an inlet or outlet. However, since the airflow is forced and the solitary wave is sufficiently far from either boundary, specific choices for lateral boundary conditions do not significantly affect the wind profile. The precursor simulations at all Re^* were performed to time $\tilde{t} = 1000$ with a maximum of 11 levels of grid refinement resulting in $\Delta x/h_0 = 0.0293$ which is sufficient, due to the relatively large-scale of the solitary wave and the lack of need to resolve very small-scale dynamics such as the overturn. A time of roughly $\tilde{t} \approx 800$ was sufficient for obtaining an equilibrated initial condition for the largest Re^* magnitude.

REFERENCES

Aagaard, Troels, Hughes, Michael G. & Ruessink, Gerben 2018 Field observations of turbulence, sand suspension, and cross-shore transport under spilling and plunging breakers. *Journal of Geophysical Research: Earth Surface* **123** (11), 2844–2862.

Ablowitz, Mark J. 2011 *Nonlinear Dispersive Waves: Asymptotic Analysis and Solitons*. Cambridge University Press.

Batchelor, George Keith 1967 *An introduction to fluid dynamics*. Cambridge university press.

Bell, John B, Colella, Phillip & Glaz, Harland M 1989 A second-order projection method for the incompressible Navier-Stokes equations. *Journal of Computational Physics* **85** (2), 257–283.

Blenkinsopp, C.E & Chaplin, J.R 2007 Void fraction measurements in breaking waves. *Proceedings of the Royal Society A: Mathematical, Physical and Engineering Sciences* **463** (2088), 3151–3170.

Blenkinsopp, C.E. & Chaplin, J.R. 2008 The effect of relative crest submergence on wave breaking over submerged slopes. *Coastal Engineering* **55** (12), 967–974.

Boswell, Hunter, Yan, Guirong & Mostert, Wouter 2023 Characterizing energy dissipation of shallow-water wave breaking in a storm surge. *Phys. Rev. Fluids* **8**, 054801.

Brackbill, J.U, Kothe, D.B & Zemach, C 1992 A continuum method for modeling surface tension. *Journal of Computational Physics* **100** (2), 335–354.

Bullock, G.N., Obhrai, C., Peregrine, D.H. & Bredmose, H. 2007 Violent breaking wave impacts. part 1: Results from large-scale regular wave tests on vertical and sloping walls. *Coastal Engineering* **54** (8), 602–617.

Chanson, Hubert & Jaw-Fang, Lee 1997 Plunging jet characteristics of plunging breakers. *Coastal Engineering* **31** (1), 125–141.

Deike, Luc, Melville, W Kendall & Popinet, Stéphane 2016 Air entrainment and bubble statistics in breaking waves. *Journal of Fluid Mechanics* **801**, 91–129.

Deike, Luc, Popinet, Stephane & Melville, W 2015 Capillary effects on wave breaking. *Journal of Fluid Mechanics* **769**, 541–569.

Derakhti, Morteza & Kirby, James T. 2014 Bubble entrainment and liquid–bubble interaction under unsteady breaking waves. *Journal of Fluid Mechanics* **761**, 464–506.

Douglass, Scott L 1990 Influence of wind on breaking waves. *J. Waterw. Port Coast. Ocean Eng.* **116** (6), 651–663.

Elgar, Steve & Guza, R T 1985 Observations of bispectra of shoaling surface gravity waves. *J. Fluid Mech.* **161**, 425–448.

Feddersen, Falk, Fincham, Adam M., Brodie, Katherine L., Young, Adam P., Spydell, M.S., Grimes, Derek J., Pieszka, Michal & Hanson, Kentaro 2023 Cross-shore wind-induced changes to field-scale overturning wave shape. *Journal of Fluid Mechanics* **958**, A4.

Feddersen, Falk & Veron, Fabrice 2005 Wind effects on shoaling wave shape. *J. Phys. Oceanogr.* **35** (7), 1223–1228.

Fuster, Daniel & Popinet, Stéphane 2018 An all-mach method for the simulation of bubble dynamics problems in the presence of surface tension. *Journal of Computational Physics* **374**.

Grilli, Stephan T, Svendsen, Ib A & Subramanya, Ravishankar 1997 Breaking criterion and characteristics for solitary waves on slopes. *J. Waterw. Port Coast. Ocean Eng.* **123** (3), 102–112.

Guyenne, P. & Grilli, S. T. 2006 Numerical study of three-dimensional overturning waves in shallow water. *Journal of Fluid Mechanics* **547**, 361–388.

Hao, Xuanting & Shen, Lian 2019 Wind–wave coupling study using les of wind and phase-resolved simulation of nonlinear waves. *Journal of Fluid Mechanics* **874**, 391–425.

van Hooft, J. Antoon, Popinet, Stéphane, van Heerwaarden, Chiel C., van der Linden, Steven J. A., de Roode, Stephan R. & van de Wiel, Bas J. H. 2018 Towards adaptive grids for atmospheric boundary-layer simulations. *Boundary-Layer Meteorology* **167** (3), 421–443.

Iafrati, A 2009 Numerical study of the effects of the breaking intensity on wave breaking flows. *Journal of Fluid Mechanics* **622**, 371–411.

Jeffreys, Harold 1925 On the formation of water waves by wind. *Proc. R. Soc. Lond. A* **107** (742), 189–206.

Johansen, Hans & Colella, Phillip 1998 A Cartesian grid embedded boundary method for Poisson's equation on irregular domains. *Journal of Computational Physics* **147**, 60–85.

Keulegan, Garbis H 1948 Gradual damping of solitary waves. *J. Res. Natl. Bur. Stand* **40** (6), 487–498.

Knowles, Jeffrey & Yeh, Harry 2018 On shoaling of solitary waves. *J. Fluid Mech.* **848**, 1073–1097.

Leykin, I A, Donelan, M A, Mellen, R H & McLaughlin, D J 1995 Asymmetry of wind waves studied in a laboratory tank. *Nonlinear Process Geophys.* **2** (3/4), 280–289.

Liu, Shuo, Wang, Hui, Bayeul-Lainé, Annie-Claude, Li, Cheng, Katz, Joseph & Coutier-Delgosha, Olivier 2023 Wave statistics and energy dissipation of shallow-water breaking waves in a tank with a level bottom. *Journal of Fluid Mechanics* **975**, A25.

Longuet-Higgins, M. S. 1982 Parametric solutions for breaking waves. *Journal of Fluid Mechanics* p. 403–424.

Lubin, Pierre, Kimmoun, Olivier, Véron, Fabrice & Glockner, Stéphane 2019 Discussion on instabilities in breaking waves: vortices, air-entrainment and droplet generation. *European Journal of Mechanics-B/Fluids* **73**, 144–156.

Lubin, Pierre, Vincent, Stéphane, Abadie, Stéphane & Caltagirone, Jean-Paul 2006 Three-dimensional large eddy simulation of air entrainment under plunging breaking waves. *Coastal Engineering* **53** (8), 631–655.

López-Herrera, J.M., Popinet, S. & Castrejón-Pita, A.A. 2019 An adaptive solver for viscoelastic incompressible two-phase problems applied to the study of the splashing of weakly viscoelastic droplets. *Journal of Non-Newtonian Fluid Mechanics* **264**, 144–158.

Miles, John W 1957 On the generation of surface waves by shear flows. *J. Fluid Mech.* **3** (2), 185–204.

Mostert, Wouter & Deike, Luc 2020 Inertial energy dissipation in shallow-water breaking waves. *J. Fluid Mech.* **890**, A12.

Mostert, W., Popinet, S. & Deike, L. 2022 High-resolution direct simulation of deep water breaking waves: transition to turbulence, bubbles and droplets production. *Journal of Fluid Mechanics* **942**, A27.

O'Dea, Annika, Brodie, Katherine & Elgar, Steve 2021 Field observations of the evolution of plunging-wave shapes. *Geophysical Research Letters* **48** (16), e2021GL093664.

Peregrine, D H 1983 Breaking waves on beaches. *Annual Review of Fluid Mechanics* **15** (1), 149–178.

Phillips, Owen M 1957 On the generation of waves by turbulent wind. *J. Fluid Mech.* **2** (5), 417–445.

Popinet, Stéphane 2003 Gerris: a tree-based adaptive solver for the incompressible euler equations in complex geometries. *Journal of Computational Physics* **190** (2), 572–600.

Popinet, Stéphane 2009 An accurate adaptive solver for surface-tension-driven interfacial flows. *Journal of Computational Physics* **228**, 5838–5866.

Popinet, Stéphane 2018 Numerical models of surface tension. *Annual Review of Fluid Mechanics* **50** (1), 49–75, arXiv: https://doi.org/10.1146/annurev-fluid-122316-045034.

Sous, Damien, Forsberg, Pernille Louise, Touboul, Julien & Gonçalves Nogueira, Guilherme 2021 Laboratory experiments of surf zone dynamics under on- and offshore wind conditions. *Coastal Engineering* **163**, 103797.

Ting, F. C. K. & Kirby, J. T. 1995 Dynamics of surf-zone turbulence in a strong plunging breaker. *Coastal Engineering* **24** (3-4), 177–204.

Ting, F C K & Kirby, J T 1996 Dynamics of surf-zone turbulence in a spilling breaker. *Coastal Engineering* **27** (3-4), 131–160.

Wroniszewski, Paweł A, Verschaeve, Joris CG & Pedersen, Geir K 2014 Benchmarking of Navier–Stokes codes for free surface simulations by means of a solitary wave. *Coastal Engineering* **91**, 1–17.

Wu, Jiarong & Deike, Luc 2021 Wind wave growth in the viscous regime. *Phys. Rev. Fluids* **6**, 094801.

Wu, Jiarong, Popinet, Stéphane & Deike, Luc 2022 Revisiting wind wave growth with fully coupled direct numerical simulations. *Journal of Fluid Mechanics* **951**, A18.

Xie, Zhihua 2014 Numerical modelling of wind effects on breaking solitary waves. *Eur. J. Mech. B Fluids* **43**, 135–147.

Xie, Zhihua 2017 Numerical modelling of wind effects on breaking waves in the surf zone. *Ocean Dyn.* **67** (10), 1251–1261.

Yasuda, Takashi, Mutsuda, Hidemi, Mizutani, Natsuki & Matsuda, Hirofumi 1999 Relationships of plunging jet size to kinematics of breaking waves with spray and entrained air bubbles. *Coastal Engineering Journal* **41** (3-4), 269–280.

Zdyrski, Thomas & Feddersen, Falk 2020 Wind-induced changes to surface gravity wave shape in deep to intermediate water. *J. Fluid Mech.* **903**, A31.

Zdyrski, Thomas & Feddersen, Falk 2021 Wind-induced changes to surface gravity wave shape in shallow water. *J. Fluid Mech.* **913**, A27.

Zdyrski, Thomas & Feddersen, Falk 2022 Wind-induced changes to shoaling surface gravity wave shape. *Phys. Rev. Fluids* **7**, 074802.